CENTRO DE INVESTIGACIONES EN ÓPTICA, A.C.

SUPER-RESOLUTION IN OPTICAL SYSTEMS

Dissertation Submitted in Partial Fulfillment of the Requirements for the Degree of Doctor of Science (Optics)

"Versión definitiva. ***Incluye cambios sugeridos por revisores"***

Adviser: Dr. Noé Alcalá Ochoa

Student: Ninfa del Carmen Lozano Rincón

December, 2017
León, Guanajuato, México

Approval

Name:	**Ninfa del Carmen Lozano Rincón**
Degree:	**Doctor of Sciences (Optics)**
Title:	***Super-resolution in Optical Systems***
Examining Committee:	**Chair:** Dr. Noé Alcalá Ochoa Professor

Dr. Carlos Pérez López
Internal Examiner
Professor _____

Dra. Maria del Socorro Hernández Montes
Internal Examiner
Professor _____

Dr. Donato Luna Moreno
Internal Examiner
Professor _____

Dr. Bernardino Barrientos García
Internal Examiner
Professor _____

Dr. Francisco Javier Casillas Rodríguez
External Examiner
Professor
CU Lagos UDG _____

Date Defended: December, 2017

Abstract

Imaging is a fundamental piece for distinct knowledge areas: object recognition, monitoring of diseases, observation of biological tissues area, astronomy, etc. In fact, many clinical advances have been through imaging techniques. Owing to these applications, improvement of imaging is of great importance.

In this work, we deal with the improvement of imaging through the analysis of the spatial resolution of lenses in order to enhance their performance. The main objective of this thesis project was to generate super-resolution in a singlet lens through the modification of one or both surfaces of the lens. Hence, we present a method to achieve super-resolution of a lens (super-resolution is the ability of an optical system to resolve spatial structures of size smaller than the value limited by diffraction). The first task is to insure that the lens under analysis meets diffraction limited performance. This is necessary to warrant the minimum level of aberrations and a solution may be found. There are several types of aberrations, but the spherical aberration is not straightforward to be corrected. So, we carry out an analysis to design lenses without spherical aberration for a certain kind of aspherical lenses. Then, we proposed a method to design lenses with super-resolution properties.

Finally, we demonstrated that method to generate lenses with super-resolution properties works analytically and experimentally.

Keywords: Super-resolution, spherical aberration, lenses, aspherical lenses

Dedication

To whom I love very much and thanks to them I have been able to achieve many goals:

Julio Lozano Arellano and Ma. del Carmen Rincón Cruz

Acknowledgements

First, I thank God, for giving me health, strength and a life full of learnings.

I thank my thesis advisor, Dr. Noé Alcalá Ochoa for sharing his knowledge with me, thank you Doctor.

I must also thank CONACYT and the CIO, for giving me the opportunity to grow professionally.

I want to thank also to Dr. Donato Luna Moreno, Dra. María del Socorro Hernández Montes, Dr. Carlos Pérez López, Dr. Bernardino Barrientos García and Dr. Francisco Javier Casillas Rodríguez for their valuable corrections made in this work.

I want to thank to Optical workshop in Cio, especially to Fis. Carlos Pérez Santos for his support to develop this work.

I would also like to thank the engineer José Jesús Padierna García for his unconditional help.

I thank all those people who in some way contributed to the realization of this thesis.

Thank you

Contents

List of Tables

List of Figures

Chapter 1

Introduction

Technological advances continuously take place in daily life, in different fields such computation, electronic communications media, imaging, health care, etc. Those regarding imaging are mainly associated with processing and displaying of data.

Imaging is a fundamental piece for distinct knowledge areas: object recognition, monitoring of diseases, observation of biological tissues area, astronomy, etc. In fact, many clinical advances have been through imaging techniques. Owing to these applications, improvement of imaging is of great importance.

In this work, we deal with the improvement of imaging through the analysis of the spatial resolution of lenses in order to enhance their performance. We present a method to achieve super-resolution of a lens (super-resolution is the ability of an optical system to resolve spatial structures of size smaller than the value limited by diffraction). The first task is to insure that the lens under analysis meets diffraction limited performance. This is necessary to warrant the minimum level of aberrations and a solution may be found. There are several types of aberrations [2], but the spherical aberration is the only one that affects the optical axis. Since our analysis of super-resolution is done in the axis, then the aberration we work with is the spherical aberration. We take as a reference a published work where is shown a procedure to correct this type of aberration. However, the author only applies the method to spherical lenses.

Starting from here, we develop a method to design lenses with super-resolution properties of aspherical lenses. Hence, we carry out an analysis to design lenses without spherical aberration, but for aspherical lenses, which are more difficult to manufacture than spherical ones but have much better performance.

The outline of the work is as follows:

In chapter two the theoretical concepts for this thesis work are presented. Following, in chapter three the antecedents of super-resolution are included, in chapter four, we present the method to design lenses with super-resolution. The model for designing parabolic-aspherical lenses is introduced in chapter five. Finally, in chapter six we present our general conclusions and outline some guidelines for future work.

1.1 Published articles

As a result of the thesis work, the following articles was published:

Ninfa del C. Lozano-Rincón, Juan Camilo Valencia-Estrada. **Paraboloid-aspheric lenses free of spherical aberration**. Jornal of Modern Optics (2016), 1146-1157.
DOI: `https://doi.org/10.1080/09500340.2016.1266708`

Ninfa del C. Lozano-Rincón, Noé Alcalá Ochoa. **Design of super-resolving lenses in far-field imaging. Optics Communications** (2017) 316-322.
DOI: `http://dx.doi.org/10.1016/j.optcom.2016.09.026`

Chapter 2

Basic Concepts

The propagation of electromagnetic waves such as light can be described by wave equation, which is deduced from Maxwell's equations [3]. The wave equation in vacuum is

$$\nabla^2 \overrightarrow{E} - \frac{1}{c^2} \frac{\partial^2 \overrightarrow{E}}{\partial t^2} = 0 \tag{2.1}$$

where $\overrightarrow{E} = \overrightarrow{E}(x, y, z, t)$ is the electric field, (x, y, z) are cartesian coordinates and t is the variable time. For each E_x, E_y and E_z, the equation (2.1) is identical in vacuum, $\nabla^2 E_x - \frac{1}{c^2} \frac{\partial^2 E_x}{\partial t^2} = \nabla^2 E_y - \frac{1}{c^2} \frac{\partial^2 E_y}{\partial t^2} = \nabla^2 E_z - \frac{1}{c^2} \frac{\partial^2 E_z}{\partial t^2} = 0$, so they will be denoted by $\tilde{u}$ hereafter. Assuming a monochromatic wave, a solution of equation (2.1) is

$$\tilde{u}(x, y, z, t) = u(x, y, z) e^{-i\omega t} \tag{2.2}$$

where $i^2 = -1$ is the imaginary unit, ω is the frequency of the wave, $u(x, y, z)$ is the disturbance in a point situated at (x, y, z) and $e^{-i\omega t}$ is the temporary part, which is the same for all points in space. Accordingly it will be omitted.

2.1 Diffraction

Diffraction is a property of the light which can be defined like "any deviation of light rays from rectilinear paths which cannot be interpreted as reflection or refraction [4]." So, when the light passes through an aperture of the size of the order of the light, the light is diffracted, therefore u changes owing to the boundaries of the aperture. The Figure (2.1) shows the propagation of a field $u_0(x_0, y_0)$ at a distance z when light impinges on an aperture Σ. $u_0(x_0, y_0)$ situated at plane (x_0, y_0) becomes into $u(x, y)$. This, according to Huygens-Fresnel, is described in cartesian coordinates by

$$u(x, y) = \frac{z}{i\lambda} \int \int_{\Sigma} U_0(x_0, y_0) \frac{e^{ikr}}{r^2} dx_0 dy_0 \tag{2.3}$$

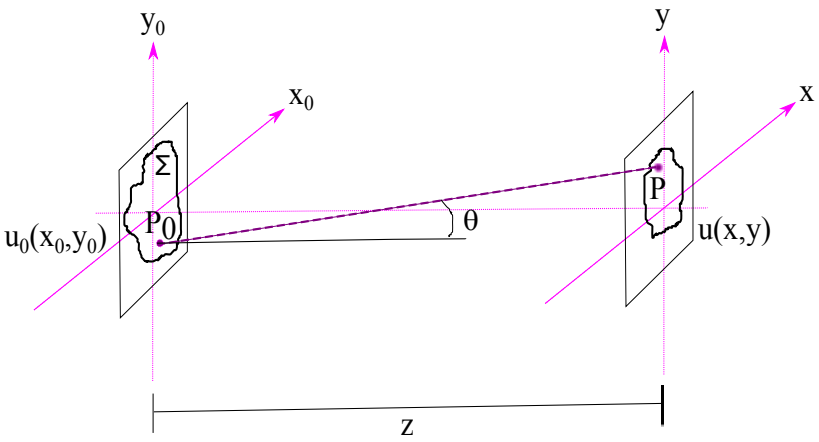

Figure 2.1: Diffraction of field u_0

where λ is the wavelength of light, $k = 2\pi/\lambda$ is the wavenumber, $r = \sqrt{z^2 + (x - x_0)^2 + (y - y_0)^2}$ is the distance between P_0 and P and $\cos\theta = z/r$.

Due that equation (2.3) is difficult to calculate for general fields and general apertures, it is necessary to perform some approximations, like those described by Fresnel and Fraunhofer, and more recently, an approximation that improve both of them [5]. For this reason, the above-mentioned approaches are described below.

2.1.1 Fresnel's formula of Diffraction

The binomial expansion states that

$$\sqrt{1+a} = 1 + \frac{1}{2}a - \frac{1}{8}a^2 + ... \qquad a < 1. \tag{2.4}$$

Now, if this expansion is applied to the expression of r

$$\begin{aligned} r = & \sqrt{z^2 + (x - x_0)^2 + (y - y_0)^2} \\ = & \sqrt{z^2\Big[1 + \frac{(x - x_0)^2}{z^2} + \frac{(y - y_0)^2}{z^2}\Big]} \\ = & z\sqrt{1 + \Big(\frac{x - x_0}{z}\Big)^2 + \Big(\frac{y - y_0}{z}\Big)^2} \\ \approx & z\Big[1 + \frac{1}{2}\Big(\frac{x - x_0}{z}\Big)^2 + \frac{1}{2}\Big(\frac{y - y_0}{z}\Big)^2\Big] \end{aligned} \tag{2.5}$$

thus

$$
\begin{aligned}
u(x,y) \approx & \quad \frac{z}{i\lambda}\int\int U_0(x_0,y_0)\frac{\exp\Big(ikz\Big[1+\frac{1}{2}\Big(\frac{x-x_0}{z}\Big)^2+\frac{1}{2}\Big(\frac{y-y_0}{z}\Big)^2\Big]\Big)}{z^2\Big[1+\frac{1}{2}\Big(\frac{x-x_0}{z}\Big)^2+\frac{1}{2}\Big(\frac{y-y_0}{z}\Big)^2\Big]}dx_0dy_0 \\
= & \quad \frac{\exp(ikz)}{i\lambda z}\int\int U_0(x_0,y_0)\exp\Big[\frac{ik}{2z}(x^2-2xx_0+x_0^2+y^2-2yy_0+y_0^2)\Big]dx_0dy_0 \\
= & \quad \frac{e^{ikz}}{i\lambda z}e^{\frac{ik}{2z}(x^2+y^2)}\int\int U_0(x_0,y_0)\exp\Big[\frac{ik}{2z}(x_0^2+y_0^2)\Big]\exp\Big[\frac{-ik}{z}(xx_0+yy_0)\Big]dx_0dy_0,
\end{aligned}
\tag{2.6}
$$

where "exp (x)" represents the exponential function of x. Finally, the following equation is known as the Fresnel's approximation for diffraction

$$
u(x,y)=\frac{e^{ikz}}{i\lambda z}e^{\frac{ik}{2z}(x^2+y^2)}\int\int_{-\infty}^{\infty}\Big\{U_0(x_0,y_0)e^{\frac{ik}{2z}(x_0^2+y_0^2)}\Big\}e^{\frac{-2\pi i}{\lambda z}(xx_0+yy_0)}dx_0dy_0, \tag{2.7}
$$

which is Fourier Transform of aperture $U_0(x_0,y_0)$ and quadratic phase function $e^{\frac{ik}{2z}(x_0^2+y_0^2)}$.

2.1.2 Fraunhofer's Formula of Diffraction

If the distance z of propagation of the field satisfies the following condition

$$
z >> \frac{k(x_0^2+y_0^2)_{\max}}{2}, \tag{2.8}
$$

it is considered diffraction in far field or Fraunhofer diffraction. Thus

$$
\frac{ik}{2z}(x_0^2+y_0^2)\to 0, \tag{2.9}
$$

which implies that the equation (2.7) changes to

$$
u(x,y)=\frac{e^{ikz}}{i\lambda z}e^{\frac{ik}{2z}(x^2+y^2)}\int\int_{-\infty}^{\infty}\{U_0(x_0,y_0)\}e^{\frac{-2\pi i}{\lambda z}(xx_0+yy_0)}dx_0dy_0, \tag{2.10}
$$

where the integral is Fourier Transform of aperture $U_0(x_0,y_0)$.

The intensity of a scalar monochromatic wave can be defined as

$$
I(x,y)\propto|u(x,y)|^2. \tag{2.11}
$$

In other words, it is proportional to the squared magnitude of the scalar field of the wave [6].

2.1.3 Fraunhofer's of Diffraction of a rectangular aperture

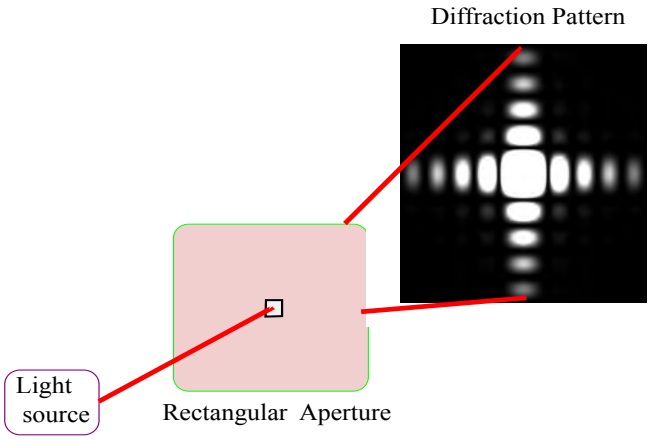

Figure 2.2: Diffraction pattern of a rectangular aperture

A plane wave passes through a rectangular aperture, as shown in Figure (2.2). If the sides of the rectangle are 2l and 2h, then the equation (2.10) for this case is

$$\begin{aligned}
u(x,y) = & \frac{e^{ikz}}{i\lambda z} e^{\frac{ik}{2z}(x^2+y^2)} \int_{-l}^{l}\int_{-h}^{h} e^{\frac{-2\pi i}{\lambda}(xx_0+yy_0)} dx_0 dy_0, \\
= & \frac{e^{ikz}}{i\lambda z} e^{\frac{ik}{2z}(x^2+y^2)} \int_{-l}^{l} e^{\frac{-2\pi i}{\lambda}(xx_0)} dx_0 \int_{-h}^{h} e^{\frac{-2\pi i}{\lambda}(yy_0)} dy_0, \\
= & \frac{e^{ikz}}{i\lambda z} e^{\frac{ik}{2z}(x^2+y^2)} \left[\frac{-\lambda}{2i\pi x}\left(e^{\frac{-2\pi i}{\lambda}xl} - e^{\frac{2\pi i}{\lambda}xl}\right)\right]\left[\frac{-\lambda}{2i\pi y}\left(e^{\frac{-2\pi i}{\lambda}yh} - e^{\frac{2\pi i}{\lambda}yh}\right)\right], \\
= & \frac{e^{ikz}}{i\lambda z} e^{\frac{ik}{2z}(x^2+y^2)} \left[2\frac{\sin(\frac{2\pi xl}{\lambda})}{\frac{2\pi x}{\lambda}}\right]\left[2\frac{\sin(\frac{2\pi yh}{\lambda})}{\frac{2\pi y}{\lambda}}\right], \\
= & \frac{4lhe^{ikz}}{i\lambda z} e^{\frac{ik}{2z}(x^2+y^2)} \left[\frac{\sin(\frac{2\pi xl}{\lambda})}{\frac{2\pi xl}{\lambda}}\right]\left[\frac{\sin(\frac{2\pi yh}{\lambda})}{\frac{2\pi yh}{\lambda}}\right]
\end{aligned} \tag{2.12}$$

Hence, the intensity is

$$I(x,y) \propto |u(x,y|^2 = \frac{4lhe^{ikz}}{i\lambda z} e^{\frac{ik}{2z}(x^2+y^2)} \left[\frac{\sin^2(\frac{2\pi xl}{\lambda})}{(\frac{2\pi xl}{\lambda})^2}\right]\left[\frac{\sin^2(\frac{2\pi yh}{\lambda})}{(\frac{2\pi yh}{\lambda})^2}\right] \tag{2.13}$$

2.1.4 Fraunhofer diffraction field of a circular aperture

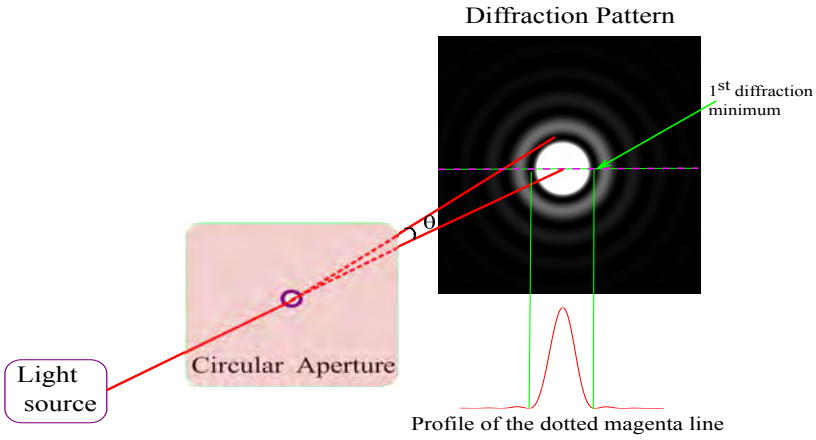

Figure 2.3: Diffraction pattern of a circular aperture

It is considered a plane wave impinging into a circular aperture as shown in Figure (2.3). The complex field immediately after the aperture plane is

$$u_0(x_0, y_0) = \text{circ}\Big(\frac{\sqrt{x_0^2 + y_0^2}}{w}\Big) \tag{2.14}$$

where w is the radius of the circular aperture and "circ" denotes a circular function, which is definited as

$$\text{circ}(\sqrt{a^2+b^2}) = \begin{cases} 1 & \text{if } \sqrt{a^2+b^2} < \frac{1}{2} \\ -\frac{1}{2} & \text{if } \sqrt{a^2+b^2} = \frac{1}{2} \\ 0 & \text{Otherwise.} \end{cases} \tag{2.15}$$

Thus, the Fourier Transform of u_0 is

$$\mathfrak{F}\left\{(u_0(x_0, y_0)\right\} = w^2 \frac{J_1\Big(2\pi w\sqrt{f_{x_0}^2 + f_{y_0}^2}\Big)}{w\sqrt{f_{x_0}^2 + f_{y_0}^2}} \tag{2.16}$$

where $f_{x_0} = x/\lambda z$, $f_{y_0} = y/\lambda z$ and J_1 is the Bessel function. Therefore, the field $u(x, y)$ is described by

$$u(x, y) = \frac{e^{ikz}}{i\lambda z} e^{\frac{ik}{2z}(x^2+y^2)} w^2 \frac{J_1(\frac{2\pi w}{\lambda z}\sqrt{x^2+y^2})}{\frac{w\sqrt{x^2+y^2}}{\lambda z}} \tag{2.17}$$

The intensity shown in diffraction pattern in Figure (2.3) is

$$I(x,y) \propto |u(x,y|^2 = \left(\frac{w^2}{\lambda z}\right)^2 \left[\frac{J_1(\frac{2\pi w}{\lambda z}\sqrt{x^2+y^2})}{\frac{w\sqrt{x^2+y^2}}{\lambda z}}\right]^2 \tag{2.18}$$

Note that the first minimum of J_1 is when

$$\frac{2\pi w}{\lambda z}\sqrt{x^2+y^2} = 1.22\pi, \tag{2.19}$$

therefore the first diffraction minimum is at 3.86.

If $y = 0$ and it is considered also angles very small (paraxial approximation), then we have $\tan\theta = \frac{x}{z} \approx \sin\theta$. Thus

$$\sin\theta \approx 1.22\frac{\lambda}{2w} = 1.22\frac{\lambda}{D} \tag{2.20}$$

where D is the diameter of the center lobe. The center lobe is known as Airy disc, which concentrates approximately 80 percent of all energy.

Considering that the optical system is free of aberrations, of which we will speak later, the ideal point image intensity of an object point with Lambertian emission characteristic illuminating the circular aperture homogeneously is called the Point Spread Function (PSF) [7]. It can be observed in Figure (2.4) that the PSF is not only an image in a plane but also is an entire volume centered in the image plane.

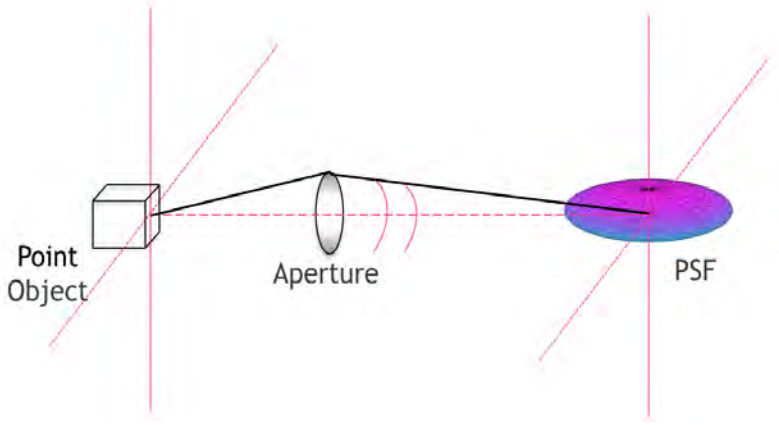

Figure 2.4: Point Spread Function of an object point

2.1.5 Alternative method to evaluate the Rayleigh-Sommerfeld diffraction

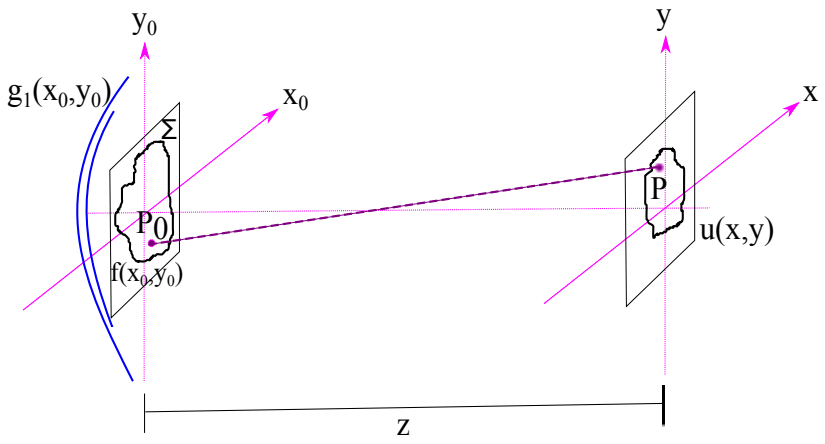

Figure 2.5: Rayleigh-Sommerfeld diffraction

Diffraction can be described by the First Rayleigh-Sommerfeld formulation (R-S) in rectangular coordinates [5], from which the formula for the complex amplitud field distribution $u_{RS}(x, y)$ can be mathematically obtained for

$$u_{RS}(x,y) = \frac{z}{2\pi}\int\int_{\Sigma} f(x_0,y_0)g_1(x_0,y_0)(ik-\frac{1}{r})\frac{e^{ikR}}{R^2}dx_0dy_0 \tag{2.21}$$

where $f(x_0, y_0)$ is an aperture function and $g_1(x_0, y_0)$ the illuminating wavefront, Σ is the diffraction aperture and R is the distance between P_0 and P. The Figure (2.5) shows the geometry for the Rayleigh-Sommerfeld diffraction. Note that $u_{RS}(x, y)$ is a function of $f(x_0, y_0)$ and $g_1(x_0, y_0)$ at a certain distance z.

Assuming that $\lambda << z$ then $1/r \approx 1/z$. This originates the Fresnel approximation given by

$$u_F(x,y) = A\int\int_{\Sigma} f(x_0,y_0)g_1(x_0,y_0)e^{\frac{ikr^2}{2z}}e^{\frac{-i2\pi(xx_0+yy_0)}{\lambda z}}dx_0dy_0, \tag{2.22}$$

where

$$A = \frac{ie^{ikz}}{\lambda z}e^{\frac{i\pi(x_0^2+y_0^2)}{\lambda z}} \quad \text{and} \quad r = \sqrt{x^2+y^2} \tag{2.23}$$

The arguments in exponential functions are considering tilting parabolas. If $z >> r$, these parabolas act like planes resulting the approximation of Fraunhofer.

Now, Alcalá [5] proposes to use the first two terms of Taylor 's formula of the expansion of R given by

$$R \approx R_n - \frac{xx_0 + yy_0}{A_z}, \tag{2.24}$$

where $R_n = \sqrt{z^2 + x^2 + y^2}$, A_z is a constant. By substituting the above in the equation (2.21) and taking $R \approx R_n$ in the denominators, the equation (2.21) is reduced to

$$u_N(x, y) = \frac{z}{2\pi} \int\int_{\Sigma} f(x_0, y_0) g_1(x_0, y_0) \Big(ik - \frac{1}{R_n}\Big) \frac{e^{ikR_n}}{R_n^2} e^{\frac{-i2\pi(xx_0+yy_0)}{\lambda A_z}} dx_0 dy_0. \tag{2.25}$$

Equation (2.25) is Fourier Transform of the pupil multiplied by other functions. Thus, we showed three different integrals to model mathematically the optical effect of diffraction.

Now, if two sources of light are considered then each of them will produce a diffraction pattern. When these sources are very close to each other, the patterns of diffraction are overlapped. So, we can not distinguish the two sources. To know more about the conditions to be able to differentiate the two sources below it is presented the issue of resolution.

2.2 Resolution

An optical parameter that describes the capacity of an optical system to separate the images of two objects that are very close is the resolving power. To analyze the concept of resolution, we will take as a reference the circular aperture, since it is one of the most common, for example the pupil in the eye.

It is considered two points as shown in Figure (2.6), each one has their Airy disc as image. If $\theta_{obj} >= \theta_{min}$ then the two objects can be distinguished. Otherwise, Airy disks overlap and appear to be the image of a single object.

The Figure (2.7) shows Airy discs of three different cases, two of them are not resolved. The last one satisfies the condition $\theta_{obj} = \theta_{min}$ and it can hardly distinguish that the Airy discs are separated. This criteria is known as Rayleigh criteria. In other words, it stats that two objects can be resolved if

$$d_{AiryDiscs} = 0.61 \frac{\lambda}{NA} \tag{2.26}$$

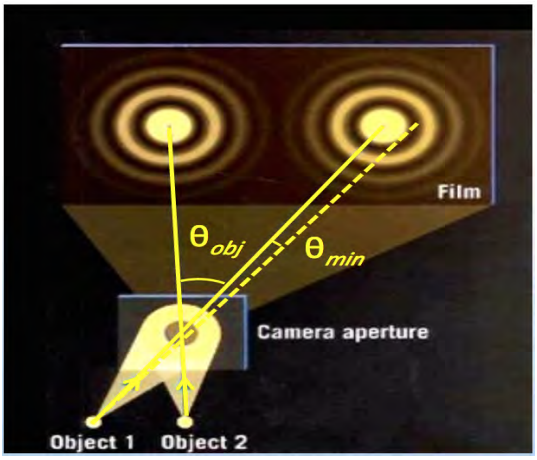

Figure 2.6: Resolution

where $d_{AiryDiscs}$ is the separation of two Airy discs and $NA = \text{n} \sin \theta$ [7].

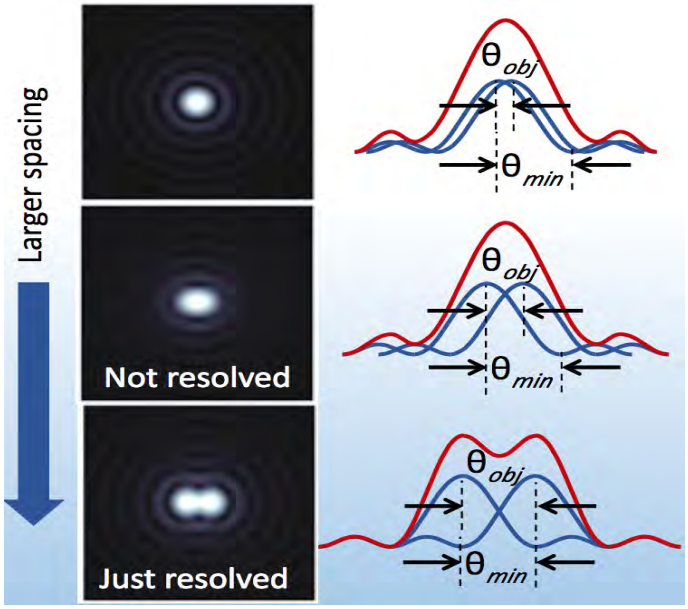

Figure 2.7: Rayleigth criteria

However, Sparrow considered that it is enough to note a little change in the intensity between the two diffraction pattern. For this case, he [8] defined d_{Airy} as

$$d_{Airy} = 0.47\frac{\lambda}{NA}. \tag{2.27}$$

.

The distance between two objects must be greater than d_{Airy}, otherwise the images can not be distinguished [9].

In the other hand, Abbe [10, 11] defined d_{Airy} as

$$d_{Airy} = 0.5\frac{\lambda}{NA}. \tag{2.28}$$

Classically, the lateral resolution for the ideal PSF is calculated by

$$\Delta x_{airy} = 0.61\frac{\lambda}{NA}, \tag{2.29}$$

which is the Airy radius. Alike the axial resolution, the depth of PSF, is usually calculated by [7]

$$\Delta z_{rayleigth} = 2\frac{\lambda}{n\sin^2\theta}. \tag{2.30}$$

The aberrations reduce the quality of the image causing the size of the PSF to increase. If it is desired to reduce it, then we must cancel or reduce the aberrations. Spherical aberration is the most difficult to reduce. This is why we will focus only on the spherical aberration, which will be described below.

2.3 Spherical aberration

Let us consider a spherical wave that is emitted by a point source and travels within an optical system. Then, wavefront is modified due several factors like the roughness of the surfaces of the optical elements, poor alignment of the optical system, changes in the medium where the light is propagated, etc.

Therefore, the presence of aberrations causes the reduction of the quality of the image. So, it is very important to correct them or avoid them. The Figure (2.8) obtained from [12] shows three different aberration which affect the diffraction pattern of a circular aperture.

Figure 2.8: Diffraction pattern in presence of spherical aberration, coma and astigmatism aberrations

There is a huge amount of research on aberrations. In this thesis project we will deal only with spherical aberration, so the fundamental concepts will only be focused on it.

Spherical aberration occurs when the rays emerging from the same point source after passing through an optical system (lens) do not converge at the same point. This happens because the rays that impinge on the edges of the lens have a greater angle of refraction while the rays that pass through the center are not refracted so much.

Figure (2.9) shows a model of a lens that generate spherical aberration while Figure (2.10) shows a lens free of spherical aberration.

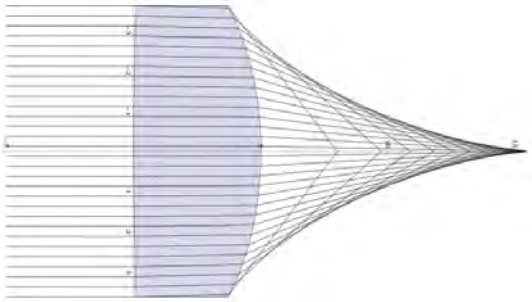

Figure 2.9: Lens that generates spherical aberration

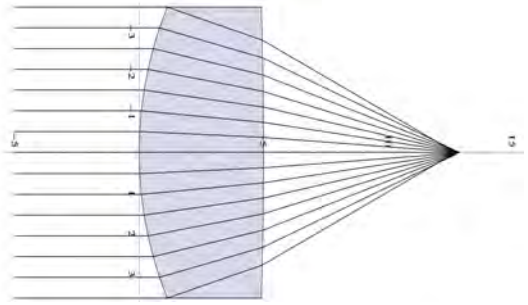

Figure 2.10: Lens free of spherical aberration

The effect of the wavefront aberrations affects the quality of the optical image formation . A parameter to measure this effect is called Strehl ratio, which is described below.

2.4 Strehl Ratio

The values of this parameter are between 0 and 1. If the wavefront is free of aberrations then Strehl ratio is 1.
By definition, Strehl ratio is the ratio of the peak diffraction intensities of an wavefront with aberrations and perfect wavefront. In other words

$$\text{Strehl Ratio}_{\text{rayleigh}} = \frac{I}{I_0}. \tag{2.31}$$

where I_0 is the peak of PSF in absence of aberrations and I is the peak of PSF with aberrations.

2.5 Super-resolution

It can be defined as the resolution improvement beyond the classical resolution limits without modifying n, λ, NA.

There are different schemes to achieve super-resolution [13]:

1.-Sharpen up the PSF, while the spatial frequency bandwidth remains unchanged.

2.-Increasing spatial frequency bandwidth, but less than $2n/\lambda$(coherent wave) or $4n/\lambda$ (incoherent wave).

3.- Increasing spatial frequency bandwidth without restriction by using digital deconvolution with constraints. It works with nonlinear imaging.

We work with the method explained above in the number 1. Superresolvings pupils work with this principle. The disadvantage of this method is that side-lobes increase their intensity, resulting in the reduction of field of view.

Chapter 3

Background of Super-resolution

Methods of super-resolution have been applied to various optical techniques. In this chapter we will explain the application of super-resolution methods to some of these optical techniques, such as

1.- Optical Microscopy.
2.- Holography.
3.- Speckle techniques.

3.1 Optical Microscopy

The improvement of the resolution began in the early 1990s by applying it in microscopy field. In the twentieth century, the resolution was limited to a spot with 200 nm diameter and axial resolution of 400-700 nm for far-field light microscopes [9].

So, it is important to know a background of microscopy.

The resolution of a microscope depends on the objective of the microscope. Regardless if a more powerful eyepiece is used, then the only thing that is achieved is an amplification, but the resolution stays unchanged. Remembering a microscope has objective and ocular, the amplification is given by the multiplication of the power of the eyepiece by the objective.

Thus, the resolution depends on the numerical aperture NA of the microscope, which is about half the diameter of the disk of Airy.

Lewis [14] gives an overview of the optical microscopy, which is summarized in Figure (3.1).

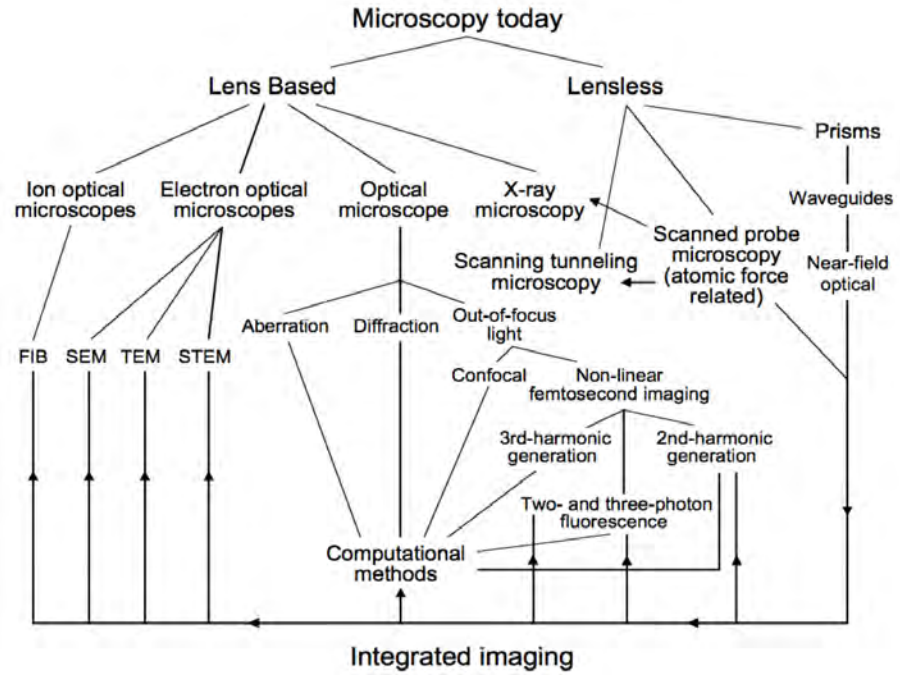

Figure 3.1: Summary of microscopy

Gustafsson [15] improved the resolution in Structured Illumination Microscopy (SIM). The method is based in Moirè technique.

Simply he takes a sample, which can be considered to be formed by a set of diffraction gratings that emit light at different frequencies. The fact of projecting a known frequency on it causes a Moirè pattern to be formed, so if we multiply cos ϕ x cos θ, multiplication gives us a high frequency term. The frequencies that the microscope objective fails to solve by being out of its resolution are taken to the center, are reduced to low frequency and therefore are solvable.

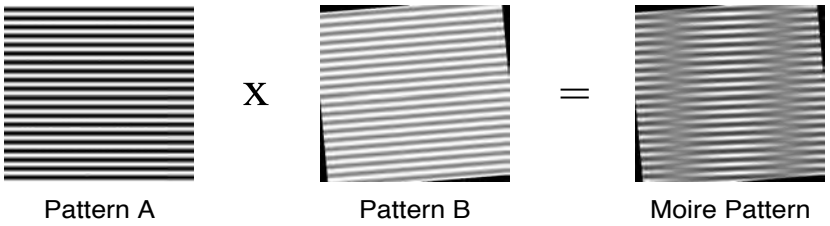

Figure 3.2: Moirè Technique

This method requires a set of images and it is sensitive to the direction of the illumination grid. Therefore it is necessary to rotate and make an overlap of the images.

To achieve super-resolution, Hell [16] illuminates a sample with two microscope lenses found. The beam of light enters on one side and recombines with light coming from the other side. The function of this microscope consists to sample and separate the PSF, as if it were multiplied by a grating. The disadvantage is that the resolution depends on the central width, but the secondary lobes increase their intensity, causing the contrast to be reduced and images lose contrast as well. Likewise, the sample must be digitally rotated and processed.

The table 3.1 shows a description of some microscopy techniques outlined by Hell [9]. These techniques have been used fluorescent particles to improve resolution. The fluorescent particles are illuminated in a certain wavelength and they emit light in other wavelength improving the resolution.

The table 3.2 presents the best resolution axial (Z) and best resolution transversal (XY) for some fluorescence microscopy methods [17].

Table 3.1: Description of Microscopy Techniques

Name of Technique	Description
4Pi Microscopy	Improves the axial resolution in scanning far-field fluorescence three-dimensional microscopyby a factor of 3-7 using two opposing lenses of high numerical aperture. To sharpen the focalspot along the optical axis, the counterpropagating spherical wavefronts of the focused excitation light field are coherently summed at the common focal point, and the spherical wavefronts of the emitted fluorescence light field are coherently summed at the detector. Depending on the specific implementation, mathematical deconvolution of raw data is either mandatory or optional. The concept essentially expands the aperture solid angle in microscopy.

I^5M	Improves the axial resolution in wide-field fluorescence three-dimensional microscopy. The scheme is similar to 4PI microscopy. The counter-propagating excitation light field forms a flat standing wave, whereas emitted fluorescence light is collected through both lenses as spherical wavefronts that are summed at a common point of detection at a camera. Mathematical deconvolution of raw data is mandatory. It can also be combined with lateral resolution improvement in a method referred to as I^5S.
STED	STED: Stimulated emission depletion microscopy. A non-diffraction-limited form of scanning far- field fluorescence microscopy. Typically, fluorescence excitation created by a focused beam of excitation light is narrowed down in space by simultaneously applying a second spot of light for molecular de- excitation featuring a central zero. The role of the de-excitation (STED) beam is to effectively confine molecules to the ground state, thus, effectively switching off the ability of the dye to fluoresce. De-excitation occurs within the nanosecond lifetime of the fluorescent state. Because no de-excitation occurs at the central zero, the excited state is established only in the region close to the zero.
GSD	GSD: Ground state depletion microscopy. Analogous to STED microscopy. The area in which molecules can reside in the fluorescent state is narrowed down in space by transiently switching the dyes to a metastable dark state-specifically, the triplet state. The use of a dark state of micro-to millisecond lifetime reduces the intensity required for the molecular switch in comparison to STED. The concept of switching fluorophores between long-lived bright and dark states has successively been extended to switching by cis-trans isomerization and other optically induced molecular bistabilities in the concept called RESOLFT.
RESOLFT	RESOLFT: reversible saturable/switchable optically linear fluorescence transition. A generalization of STED and GSD microscopy for molecular switching, including switching of reversibly activatable proteins and organic fluorophores. Switching can be regarded as a perfect saturable transition from one state to the other. The terminology saturated transition is used in conjunction with molecular ensembles to also account for the fact that in an ensemble the population of the two states may equilibrate to fractions-say, 90% in the off state and 10% in the on state.

SPEM/SSIM	SPEM/SSIM: saturated pattern excitation microscopy or saturated structured illumination microscopy. A wide-field recording, highly parallelized scanning microscopy in which the molecules are strongly excited to the fluorescent state, depleting the ground state (that is, switched from the ground state to the fluorescent state) outside the line-shaped zeros produced by a standing wave interference pattern. To cover the field of view, the pattern is scanned across the specimen by phase-shifting the maxima of the interference pattern and reading out the fluorescence imaged onto a camera for each scanning step. Because resolution is improved only perpendicular to the line-shaped zeros, the pattern is tilted several times to cover all directions in the focal plane. Mathematical analysis of the data renders super-resolved images. Even scanning a single line-zero would give super resolution, but the use of an array of lines parallelized the process over a large area.
PALM, STORM	A PALM, STORM: (fluorescence) photoactivation localization microscopy, stochastic optical reconstruction microscopy. Switches individual molecules stochastically and sparsely on by light-induced activation and then off, to detect a bunch of m photons from a single molecule on a camera, emitted while the molecules are in the on state. Calculating the centroid of the diffraction blob produced by each molecule and registering the coordinates of each molecule produces an image consisting of individualmolecule positions.STORM has been initiated with pairs of photochromic cyanine dyes with one of themused as an activation (switch-on) facilitator.
dSTORM	dSTORM: direct STORM. A simplified version of STORM that refrains from using a special dye for activation.
GSDIM	GSDIM: ground state depletion followed by individual molecule return. Switches off by depleting the molecular ground state and shelving the dye molecules in their triplet state, as in GSD. However, unlike GSD, it uses a stochastic readout, as in PALM, STORM, FPALM and dSTORM. It differs from these stochastic methods in that the dye molecule is not optically activated but is automatically switched on after its spontaneous return from the dark (triplet) state to its singlet state.
PAINT	PAINT: point accumulation. A method in which the on state is generated by the binding of something to the structure to be imaged, and the off state by free diffusion or another dark (bleached) state.

Table 3.2: Best resolution in some Fluorescence Microscopy Methods

Name of Technique	Best resolution in nm
4Pi Microscopy	$\approx 200(XY)$ $\approx 90(Z)$
I^5M	$\approx 230(XY)$ $\approx 90(Z)$
Confocal	$\approx 180(XY)$ $\approx 500(Z)$
Widefield	$\approx 230(XY)$ $\approx 1000(Z)$
PALM, STORM	$\approx 20(XY)$
2 Photon	$\approx 200(XY)$ $\approx 400(Z)$
Stimulated emission depleiton	$\approx 20(XY)$ $\approx 50(Z)$
Structured illumination	$\approx 100(XY)$

3.2 Holography

In the area of holography, Mico [18] used a very similar method to Structured Microscopy. A Mach-Zender interferometer is used with a microscope objective. The variant with respect to projecting structured light is that one has a beam splitter, some mirrors and the sample. This last is illuminated at a certain inclination.

Remembering that, if two plane waves interfere, then it is possible to get interference patterns. These consist of straight lines whose direction depends on the incident beams. Therefore it is a variant of the method of Structured Illumination and the same has the same characteristics of rotating the object or the lighting system in different directions to have sensitivity. As a hologram, it can be reconstructed digitally. That means that the hologram is known, which can be reconstructed in different planes by means of Fourier transforms or propagation of the optical field. So it can be possible to have a volumetric reconstruction.

Also, Olvera achieved optical super-resolution in a Gabor Holography optical setup [1] by using a spatial light modulator (SLM). A reflection spatial light modulator is used to display super-resolving pupils. It can be observe the optical setup in Figure (3.3). A beam laser is divided in two beams: reference beam and object beam. The object beam is modifying by SLM to generate super-resolution. Besides, he used other optical setup, which is shown in Figure (3.4).

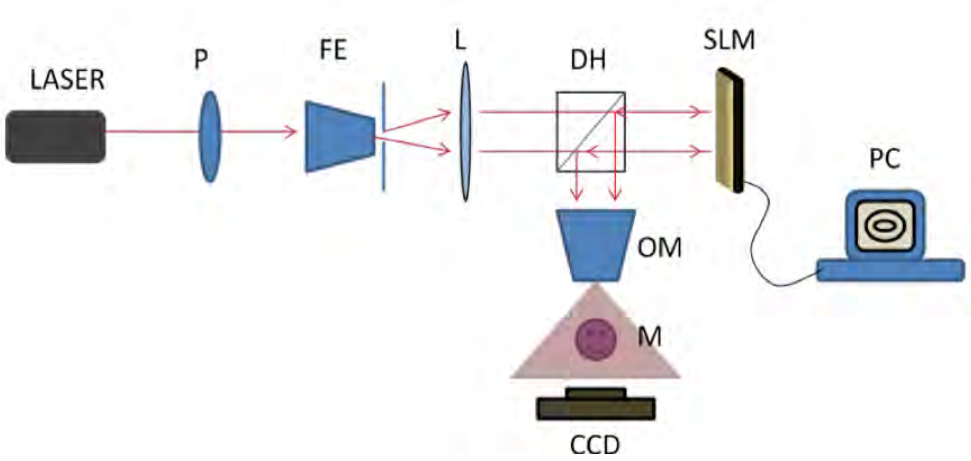

Figure 3.3: Experimental optical setup to test the super-resolution in Digital In Line Holographic Microscopy (DIHM). P- Linear Polarizer, FE- Space Filter, L-Collimating Lens, DH-Beam Divider, OM-Microscope Objective, M-Sample.

Olvera [1] obtained a reduction of PSF of 0.62 by using the complex pupil shown in figure 3.5.

The experimental PSF and its corresponding profile are shown in Figure (3.6), where the central disk was intentionally saturated in order to perform the measurement of the central disc diameter.

Finally, it was used an optical fiber like a sample. It was demonstrated that PSF was reduced by using a super-resolving pupils. The results are shown in Figure (3.7).

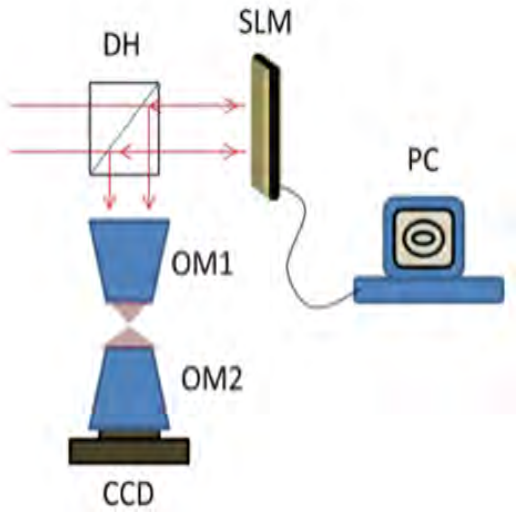

Figure 3.4: Optical setup used to check the reduction of the central disc in the diffraction pattern (focal point) of a microscope objective.

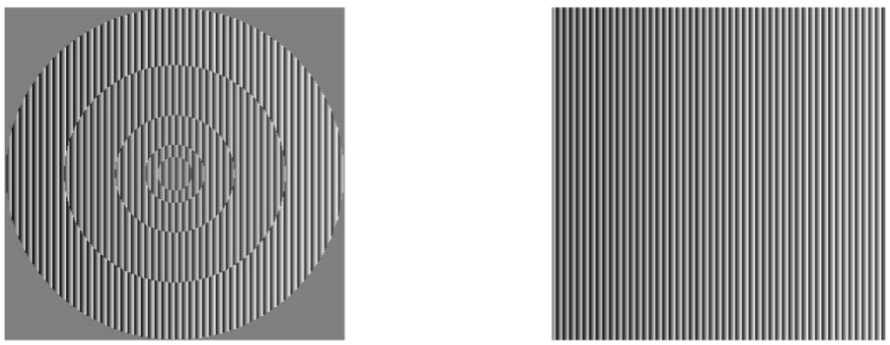

Figure 3.5: Complex pupil (left) and free pupil (right).

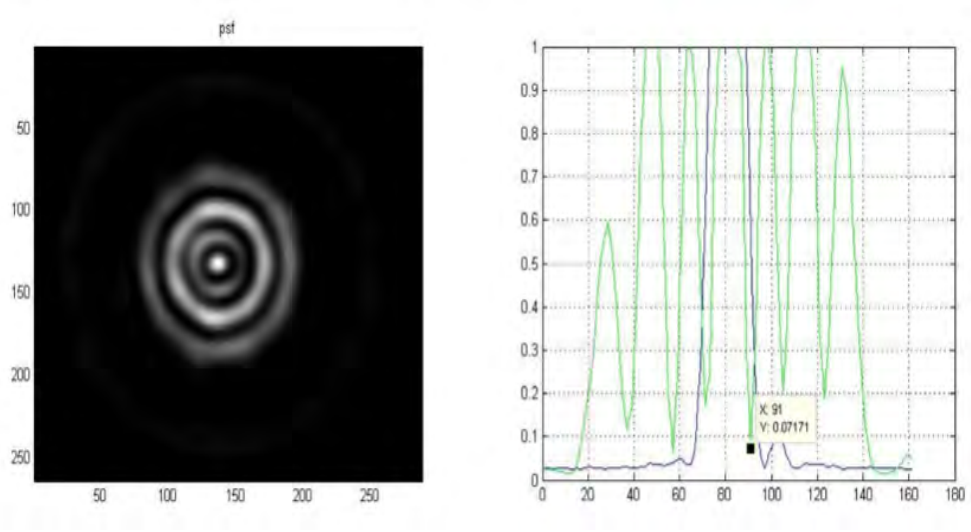

Figure 3.6: PSF (left) and its corresponding profile (right) (green) and PSF profile of the free modulated pupil (blue).

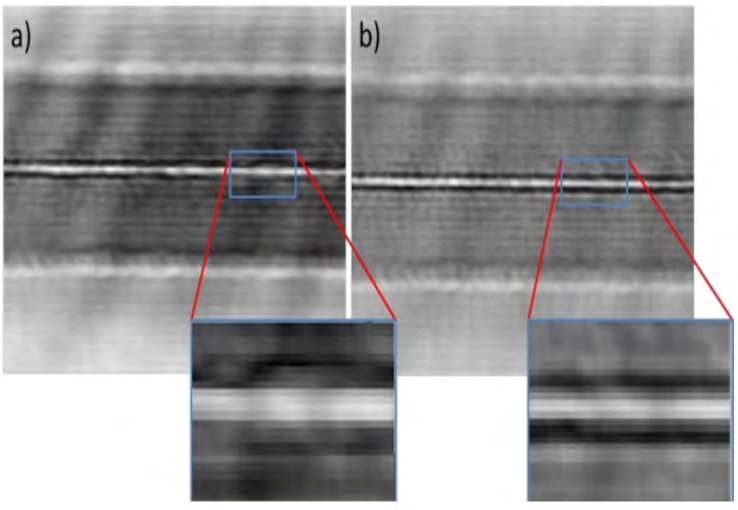

Figure 3.7: Reconstruction of core of a optical fiber using as sample in [1] a) By using free pupil, b) By using axicon pupil.

3.3 Speckle techniques

An interferometer is a device which can be recombined light, preferably coherent light. If a quasi-monochromatic source as a laser illuminates an optically rough surface, the light on the surface has a granular appearance, where areas of maximum and minimum illumination can be noted, randomly scattered throughout the illuminated surface. The height variations of this surface are of the order or larger than the wavelength λ of the laser. To this effect it is known like Speckle [19].

By making a Moiré pattern in this way with Speckle, it can retrieve the low frequency term as in the case of structured light. Different optical setups can be designed depending on the strain vector. It can be in plane, in the direction perpendicular or out of plane or a combination of all.

Then, there are two patterns of interference: one of reference and other with deformation. When subtraction is done between them, there is a low frequency phase term and a high frequency term. In fact it is double the original. Then a method is applied to determine the phase and reconstruct the difference of them.

In a paper of Chiang [20], he developed a method to improved resolution. It is very similar to the methods described above. However in this work we have the mottled analysis pattern with the microscope objective in the visible region and in a Transmission Electron Microscope (TEM).

By means of TEM, images are obtained, with which speckle patterns can be generated. It can get the field in plane from speckle patterns, in some direction or even detect fractures.

In a paper of Zheng [21], the 4pi interferometer was combined with a coherent light in two different states: one with no sample and another with sample, thus achieving super-resolution.

Chapter 4

Design of super-resolving lenses in far-field imaging

Making a lens that produces perfect images means the reduction of aberrations down to levels limited by diffraction. A diffraction limited optical system is one whose Point Spread Function (PSF) has been reduced to a minimum according to certain criteria like those laid out by Strehl, Rayleigh or Sparrow [6]. Among all aberration reductions, the spherical one is particularly important, given that for a particular wavelength, the image of an object on the optical axis is perfect if it is free from spherical aberration. Usually, lenses which do not introduce spherical aberration for a particular object and image positions on the optical axis have been designed using ray tracing, although some designs with analytical formulas have been reported, such as the Cartesian ovals of revolution [22] and other aspheric elements [23]-[24].

An important result was published several years ago by Toraldo Di Francia, which showed that there is no limit to the central peak reduction of the PSF, at the cost of increasing the secondary side lobes and reducing the central core intensity dramatically [25]. Super- resolution methods deal with the PSF core reduction of optical systems limited by diffraction, the side lobes height reduction with respect to the central lobe height, and the optimization of the Strehl ratio [26]. To achieve such super-resolution amplitude, only-phase or complex masks have been designed to modify the profile of the illuminating beam [27].

According with the revision of Lindberg, there are different schemes of super-resolution [28]. In this work we will follow one of them, which consists in sharpening up the point-spread function while the spatial frequency bandwidth remains unchanged. This way we can obtain moderate super-resolution compared with those obtained by methods that use near field information. Far field techniques hold advantages like not needing scanning devices and the ability to image without physical contact between the measuring system and the

object under analysis.

In this work [29], we show that aspherical lenses can be modified to obtain a PSF with super- resolution characteristics. We will exposit a method to obtain analytical formulas to describe the super-resolving optical elements. We will prove those formulas theoretically, using different kinds of lenses, such as a plano-hyperboloid lens, a spherical-aspherical lens and others.

From the theoretical and practical points of view, it would be interesting to have these kinds of super-resolving lenses, since different applications, such as confocal microscopy, astronomy, optical data storage, light concentrators and others, would benefit from design improvements, [30]-[31]. Additionally, there are various advantages of fabricating such super-resolving lenses; for example, spatial light modulators (SLM) can be avoided as displaying masks to add the super-resolving properties to lenses, flicker phenomena that appear from the superposition of images coming from two or more SLMs would no longer exist [32], diameter of super-resolving lenses can be larger than that permitted by the size of spatial light modulators or small enough such that the spatial resolution properties of the SLM cannot display accurately the super-resolving masks. Fabrication of lenses to work with high power lasers or wavelengths not supported by spatial modulators could be also achieved, etc.

To our knowledge, this is the first time that a method is presented to design super-resolving lenses using the manipulation of the asphericity of the optical elements surfaces. There is a work where an aspheric lens for terahertz imaging with sub-wavelenght resolution is reported [33]. Its design is based on the optimization of the reflection losses of the two lens surfaces. Although the authors have shown that the PSF spot size is about 20% smaller than that obtained with a diffraction limited system, they did not find an analytical expression for the surface lens, nor did they find super-resolution with a plano-hyperboloid lens (as we found in this work). Moreover, from the figures reported in their article, it seems that the PSF reductions were due to increments of the numerical aperture of the lenses instead of manipulations of the lenses and illumination amplitudes.

In the following sections we describe a method to calculate the PSF of an aspheric lens and our proposal to modify the aspheric surfaces of the lens in order to achieve the super-resolution; later, we present some theoretical results that validate our proposal; and finally, the discussion and conclusions of this work are given.

4.1 Method to design super-resolving lenses

We applied geometrical optics to trace the wavefront from the incident plane to the second surface of the lens. The wavefront profile at the second lens surface is used as the input of the Rayleigh-Sommerfeld scalar diffraction formula. A similar method has been used in [33] to design and build their lens. This way, a thick lens can be represented by the phase function given by

$$g(r) = e^{ikt_c} e^{ik(n_l - n_a)t(r)} \tag{4.1}$$

where $t(r)$ is the lens axial thickness at abscissa $r = \sqrt{x^2 + y^2}$, t_c is the center thickness of the lens, n_l and n_a with $n_a < n_l$ are the refractive indexes of the lens and its surrounding media, respectively; and $k = 2\pi/\lambda$, where λ is the light wavelength. We calculate the thickness function $t(r)$ using ray-tracing theory assuming rotationally symmetrical lenses. This ray tracing model obeys rigorous geometrical optic laws and applies to a single lens with anterior surface $z_a(r)$ and posterior $z_b(r)$ surface. The ideal optical system of such a lens has an object-point on the optical axis z with a vertex-object distance t_a (see figure 4.1 for notation used). From such point departs a ray that reaches an arbitrary point $(r_a, z_a(r_a))$ on the first surface, where it is refracted according to Snell's law. This ray arrives at the back surface at a point $(r_b, z_b(r_b))$ on the second surface, where the ray is again refracted. Thus, the thickness function is given by

$$t(r) = \left\{ [r_b - r_a]^2 + [Z_a(r_a) - Z_b(r_b)]^2 \right\}^{\frac{1}{2}} . \tag{4.2}$$

The Figure (4.1) shows a draw of a lens, which has two surfaces: Z_a and Z_b.

Assuming that both surfaces are known and correspond to an aspherical lens free of spherical aberration on axis, we can represent them through the Schwarzchild formulas

$$Z_a(r) = \frac{c_a r^2}{1 + \sqrt{1 - (K_a + 1)(cr^2)}} + \sum_{j=2}^{\infty} A_{2j} r^{2j} \tag{4.3}$$

$$Z_b(r) = \frac{c_b r^2}{1 + \sqrt{1 - (K_b + 1)(cr^2)}} + \sum_{j=2}^{\infty} B_{2j} r^{2j} \tag{4.4}$$

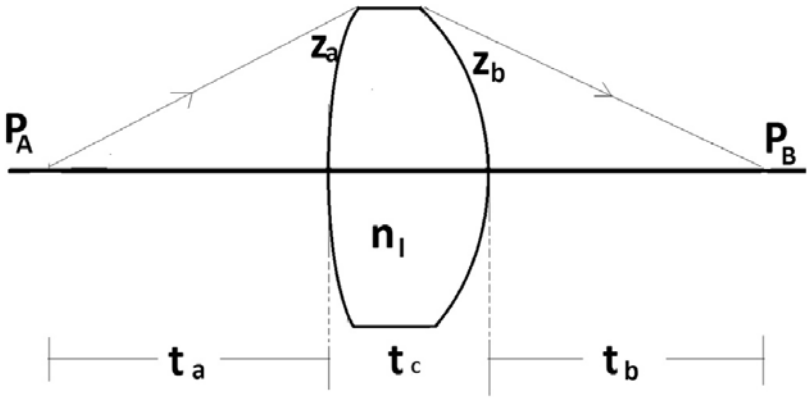

Figure 4.1: An aspheric-aspheric lens showing ray tracing. A coherent monochromatic light beam is refracted by surfaces $z_a(r)$ and $z_b(r)$ to form a perfect image located at back vertex distance t_b. Central thickness t_c and point source PA and image PB positions are indicated. n_l means refraction index of the lens.

where $c_{a,b}$ are the vertex curvatures, $K_{a,b}$ the conic constants, and A_{2j}, B_{2j} the aspherics coefficients of the respective surfaces.

Once our lens is free of spherical aberrations, we can modify the first surface or the second or both to achieve super-resolution characteristics. Then, we introduce two functions (to be calculated) $\tilde{z}_a(r)$ and $\tilde{z}_b(r)$, which we call super-resolving surfaces, such that the lens with the thickness function described by

$$\tilde{t}(r) = \sqrt{\{r_b - r_a\}^2 + \{\tilde{z}_a(r_a) + z_a(r_a)] - [\tilde{Z}_b(r_b) + Z_b(r_b)]\}^2} \tag{4.5}$$

be super-resolving. The super-resolving lens would be just described by

$$\tilde{g}(r) = e^{ikt_c} e^{ik(n_l - n_a)\tilde{t}(r)} \tag{4.6}$$

We can determine $\tilde{z}_a(r)$ or $\tilde{z}_b(r)$ or both; however, to simplify the process, we found that it is enough to calculate one of them; so Equation (4.5) we will assume $\tilde{z}_a(r) = 0$.

Next, we will explain the way to determine $\tilde{z}_b(r)$ and the path we followed to compute the diffraction properties of our aspheric lenses.

4.1.1 Calculation of the lens Point Spread Function

To determine the lens image of a wave, we followed the First Rayleigh-Sommerfeld formulation (R-S), as described by [6]. The complex amplitude field distribution $G(u, v)$ of a lens function $g(x, y)$ at a certain distance t_b is given by

$$G(u,v) = \int\limits_{\sum(x,y)} \int \frac{1}{R^2} e(x,y) g(x,y) e^{jkR} dxdy \tag{4.7}$$

where (u, v) are the dimensionless image coordinates, $\Sigma(x, y)$ is the lens aperture, $e(x, y)$ (considered a constant for a distant source, i.e. a flat wave) is the function that describes the spherical wave diverging from the point source and $R^2 = [t_b^2 + (x - \lambda t_b u)^2 + (y - \lambda t_b v)^2]$, where λ means the wavelength of light. Additionally, we define $r^2 = x^2 + y^2$ and $w^2 = u^2 + v^2$. The PSF intensity is obtained as the squared modulus of Equation (4.7) when t_b is the position of the point source image.

4.1.2 Determination of the super-resolving function

The super-resolving phase function $\tilde{z}_b(r)$ is determined using an iterative procedure of four steps where some parameters are optimized through the analysis of a PSF function. The first step of the process consists in proposing the super-resolving functions. For instance, we propose

$$\tilde{z}_b(r) = b_1[1 + cos(b_2 2\pi r)]/[k(n_l - n_a)] \tag{4.8}$$

where b_1 and b_2 are parameters to be optimized. Some paraxial super-resolving pupil designs using this function have been reported in [34].

The second step consists in carrying out ray tracing on the lens, using a point source on the optical axis at position t_a , with the anterior and posterior surfaces given by $z_a(r)$ and $z_b(r) + \tilde{z}_b(r)$ (Equations (4.3), (4.4) and (4.8)) respectively. This way, we get the thickness function $\tilde{t}(r)$ given by

$$\tilde{t}(r) = \left(\{r_b - r_a\}^2 + \{z_a(r_a) - [\tilde{z}_b(r_b) + z_b(r_b)]\}^2 \right)^{\frac{1}{2}} \tag{4.9}$$

In the third step, the PSF is calculated using Equations (4.6), (4.7) and (4.9).

Finally, in the fourth step,we use an algorithm to optimize the coefficients b_1 and b_2 of Equation (4.8) so that the following super-resolution constraints on the PSF are fulfilled: (a) the spot size reduction of the central lobe by a factor $\epsilon < 1$, (b) the Strehl ratio S, and (c) the relative side-lobe intensity Ω. These constraints have been suggested in previous papers that use the paraxial approximation of Equation (4.7) [35]-[36]. We define the constraint parameters as follows:

$$\varepsilon = \frac{DS}{DS_w} \quad S = \frac{PSF(0,0)}{PSF_w(0,0)} \quad \Gamma = \frac{PSF(0,0)}{\max[PSF(u,0)]}, \text{ for } u > \varepsilon u_1 \tag{4.10}$$

where DS means diameter of the central spot, sub index w means without super-resolving function, and u_1 is the first zero of the Airy function.

We used the Nelder-Mead fitting procedure (MATLAB) as an optimization method to minimize the following merit function

$$M(u,\Gamma) = I(\varepsilon u_1, 0) + [I(u,0) - \Gamma]^2, \; for \, u > \varepsilon u_1 \tag{4.11}$$

where $I(u,v) = G(u,v)^2$ is the PSF intensity.

The processes of steps 2 and 3 are repeated until the merit function given by Equation ((4.11)) is satisfied.

It is noteworthy that we proposed Equation (4.8) as a super-resolving function for all calculations of this work, because it contains only two parameters to be optimized, and the target of this paper is to show that the method works, but it can be used other functions with more parameters to be optimized like

$$\tilde{z}_b(r) = \frac{\phi(r)}{n_l - n_a k} \tag{4.12}$$

with phase functions given, for example, by the polynomial $\phi(r) = \Sigma_{j=0}^{N_b} b_j r^j$, where b_j are the $N_b + 1$parameters to be optimized.

Next, we will demonstrate our proposal providing some examples of super-resolving lenses with different types of surfaces.

4.2 Super-resolving lenses

For these examples, we have considered the following general parameters of lens design: light wavelength of $\lambda = 633$ nm, BK7 glass with refractive index of $n_l = 1.5151$ at the above wavelength, a distance image of $t_b = 40$ mm and a lens diameter of $D = 10$ mm. This way, we have lenses with an f-number equal to $f/4$. We also contemplate the lens to be surrounded by air ($n_a = 1.0$), although other values can be chosen, and to have its central thickness given by $t_c = D/3$. Distance t_a is specified in each example, as well as the super-resolving functions.

4.2.1 Super-resolution with spherical-aspherical lenses

In this sections, we will analyze a lens with its first surface described by a sphere and a second surface described by an asphere. The locations of the point source at finite and infinite distances are examined.

According to the recent work of [37], the sags $z_a(r)$ and $\tilde{z}_b(r)$ of this type of lens, free of spherical aberration, can be calculated with the following formulas

$$z_a(r) = R_a - \sqrt{R_a^2 - r_a^2} \tag{4.13}$$

and

$$\bar{z}_b(r) = R_a - g + \left(\frac{ai + j}{c}\right)(1 - m) \tag{4.14}$$

where

$$
\begin{aligned}
a = &\quad n_l^2, \\
b = &\quad R_a^2, \\
c = &\quad a^2 - 1, \\
d = &\quad r_a^2, \\
e = &\quad cd, \\
f = &\quad R_a - t - t_b, \\
g = &\quad \sqrt{b - d}, \\
h = &\quad n_l t + t_b - R_a + g, \\
i = &\quad ag, \\
j = &\quad i + (a+1)\sqrt{ab - d}, \\
k = &\quad -f + g + j - ah, \\
l = &\quad af + h,
\end{aligned}
\tag{4.15}
$$

where n_l, n_a, t_a, t_b, t are known parameters that have the meaning already explained; $r_a = D/2$ and R_a means the radius of curvature of the first spherical surface.

In order to write $\tilde{z}_b(r)$ as a continuous function, we have calculated Equation (4.14) for discrete values of r, and with a least squares technique, fitted it to the following polynomial of N-degree

$$
z_b(r) = \sum_{j=0}^{N} B_j r^j \tag{4.16}
$$

The degree of the polynomial N has been chosen such that the error between the fitted function $z_b(r)$ and the data $\tilde{z}_b(r)$ and the data be lower than $\lambda/8$ to assure the diffraction limit [38]. Equation ((4.16)) can be expressed like Equation (4.4) as we explained before.

After having determined sagittas $z_a(r)$ and $z_b(r)$, the super-resolving surface $\tilde{z}_b(r)$ was optimized according to the procedure described in (4.1.2). We set the constraints to be: PSF reduction factor of $\epsilon = 0.64$, moderate side lobes of $\Omega = 5$, and left the Strehl ratio unconstrained.

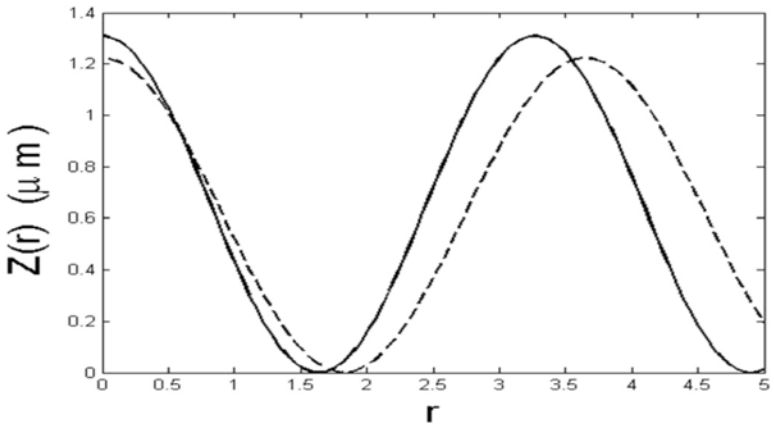

Figure 4.2: Super-resolving sags $z_b(r)$, where continuos line represents Eq. (4.17) and dashed line Eq. (4.18)

After applying our procedure to the case $t_a = -\infty$ and $R_a = 5D = 50\,\text{mm}$ (biconvex lens), we obtained the super-resolving function given by

$$\tilde{z}_b(r) = 3.125\frac{[1 + cos(\frac{2.74\pi r}{a})]}{kn_l} \tag{4.17}$$

and after repeating the process for a plano-convex lens with $t_a = -2t_b$ (another value can be chosen) and $R_a = -\infty$, we have obtained

$$\tilde{z}_b(r) = 3.345\frac{[1 + cos(\frac{3.06\pi r}{a})]}{kn_l} \tag{4.18}$$

These functions can be observed in the Figure (4.2), where a maximum sag value of about 1.3 m is obtained.

The two reference PSF's were calculated using the respective functions $z_a(r)$ and $z_b(r)$, setting $\tilde{z}_b(r) = 0$ for each case.

The corresponding PSF profiles can be observed in Figure (4.3), where the super-resolution is clearly observed for both cases. We obtained $\epsilon = 0.68$,$\Omega = 5$ and $S \approx 0.23$.

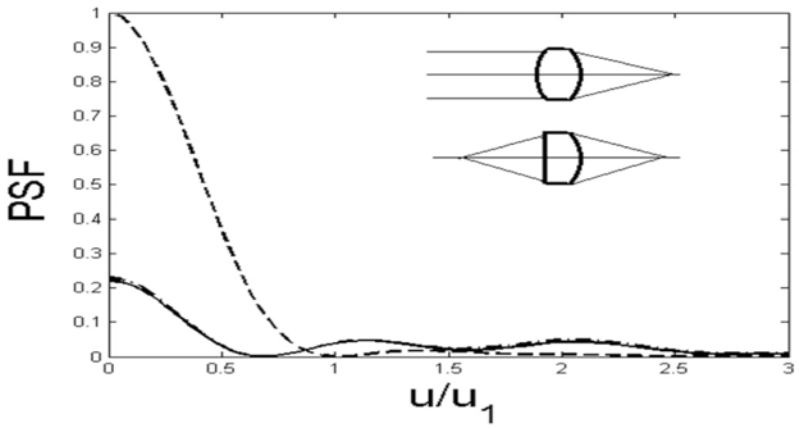

Figure 4.3: PSF's of a biconvex spheric-aspheric lens using a super-resolving sag for point source at infinity (continuous), and a plano-convex lens using a point source at a finite distance (dashed-dotted). Dashed lines represent the diffraction limit for each case. u_1 is the first zero position of the dashed line. Note that the continuous and dashed-dotted lines are almost superimposed.

4.2.2 Super-resolution with plano-hyperboloid lenses

In this section, we will analyze the lens whose first surface is given by a flat and the second one given by an asphere.

When the point source is placed on the optical axis at $t_a = -\infty$, no ray tracing is necessary to perform the optimization process, since the height of any ray on the anterior and the back surfaces remains equal; we simply use the respective sags to calculate the respective thickness function. Without the super-resolving sag, the thickness function is given by

$$t(r) = z_b(r_a) \tag{4.19}$$

and including $\tilde{z}_b(r)$, it is expressed by

$$t(r) = \tilde{z}_b(r_a) + z_{\cdot}(r_a) \tag{4.20}$$

The function $z_b(r)$ can be calculated using the formulas given in [24], where it is shown that the back surface of a lens with a flat as its first surface, for an object at infinity, and

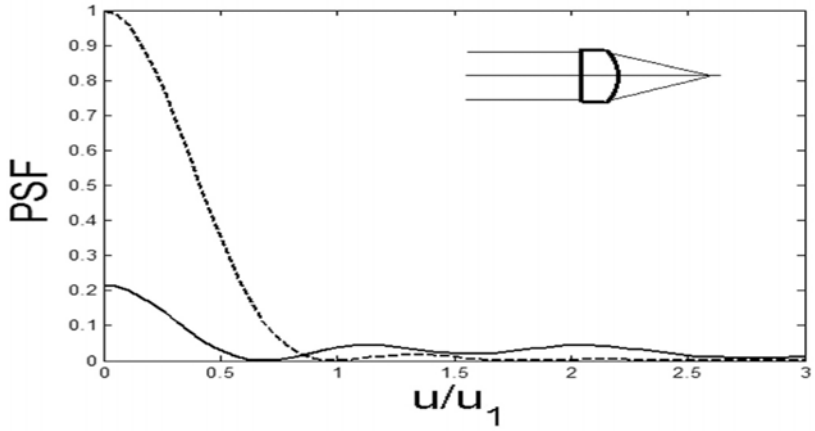

Figure 4.4: PSF of a plano-hyperboloid lens with point source at -∞. Dashed line represents the diffraction limit. Upper curve represents the super-resolving function profile in micrometers. u1 is the first zero position of the dashed line.

free of spherical aberration, is given by an hyperboloid with a vertex curvature c_b and a conical constant K_b that correspond to

$$c_b = -\frac{n_a}{f_b(n_l - n_a)} \text{ and } K_b = -\left(\frac{n_l}{n_a}\right)^2 \tag{4.21}$$

Another alternative in order to obtain $z_b(r)$ is to use the formulas of Equations (4.13), (4.14) and (4.15) as we did in the previous section, setting the radius of curvature of the sphere to $R_a = \infty$ and $t_a = -\infty$.

For the super-resolving function $z_b(r)$, we have considered that of Equation (**??**), which as mentioned before, we will design to have a PSF reduction factor of $\epsilon = 0.64$ and a secondary lobule ratio of about 5. Using the thickness function given by Equation (4.20) and calculating its PSF through the procedure explained in our first example, the expected super-resolution is obtained and it is shown in Figure (4.4).

This kind of lens is interesting because using two plano-hyperboloid lenses we can build a new lens working as finite-conjugated and free of spherical aberration. We can apply our super-resolving process to the hyperboloid-hyperboloid lens in a way similar to what we did in section 4.2.1.

Another interesting configuration, due to its robustness with off-axis aberrations, is when the first surface is a flat ($z_a(r) = 0$), the point source is at finite a distance, and the image is at $t_b = \infty$; that is, the flat surface faces the curved wavefront. We have achieved super-resolution setting the super-resolving function indistinctly in any of the two surfaces.

4.2.3 Super-resolution with an ellipse and a concave sphere

We have included a lens of this type since the formulas of section 4.2.1 are useful only when the first surface is a sphere.

As in the plano-hyperboloid case, it can be found again in reference [24] that the first surface of an aspheric lens, free of spherical aberrations, with the back surface given by a sphere of radius $R_b = t_b$, for a point source at $t_a = -\infty$ and an image at a finite position $t_b < \infty$, has a vertex curvature c_a and a conical constant k_a that correspond to the ellipsoid

$$C_a = \frac{n_l}{(t_b + t_c)(n_a - n_l)} \quad \text{and} \quad K_a = -\left(\frac{n_a}{n_l}\right)^2 \tag{4.22}$$

$z_b(r)$ is obtained from Equations. (4.4) and (4.22).

In the same fashion as in prior examples, we chose the second surface to be the super-resolving one. Following our optimization procedure, with $t_b = 4D$, we found the super-resolving function given by

$$\tilde{z}_b(r) = 3.03\frac{[1 + \frac{cos(2.46\pi r)}{a}]}{kn_l} \tag{4.23}$$

and the respective PSF is observed in the figure 4.5, with the expected super-resolution.

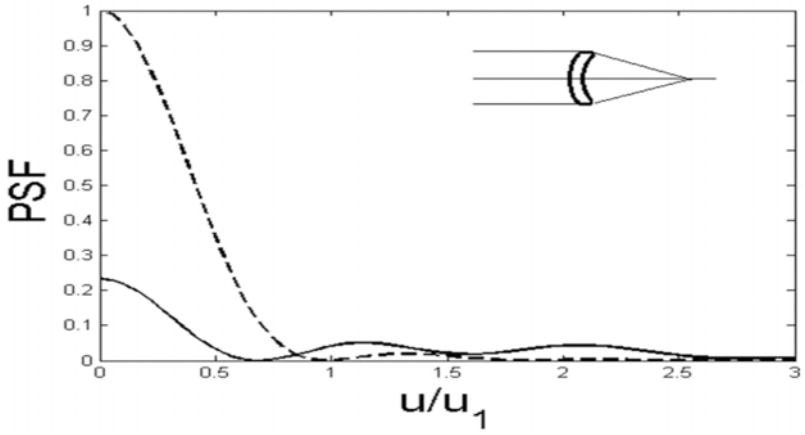

Figure 4.5: PSF of a lens with its first surface given by an ellipse and a second surface given by a concave sphere. Dashed line represents the diffraction limit. u_1 is the first zero position of the dashed line

4.3 Method to design super-resolving mirrors

Although we have focused on super-resolving lenses, with minor changes to our procedure, we can also attain super-resolving mirrors. The mirrors can be represented by the phase function given by

$$g_m(r) = e^{ikt_{cm}} e^{ikt_m(r)} \tag{4.24}$$

where $t_m(r)$ is the thickness function of the mirror given by the optical path function at the abscisa r , and t_{cm} is a constant related with the image distance from the mirror vertex . As in the description given before, we have calculated the function $t_m(r)$ using the ray-tracing theory while assuming rotationally symmetrical mirrors. The ideal optical system of such a lens would have an object-point on the optical axis z with a vertex-object distance t_a (see figure 4.6 for the notation used). From such point departs a ray that reaches an arbitrary point $(r_m, z_m(r_m))$ on the mirror's surface, where it is reflected according to the laws of reflection. This ray arrives at the image position $(r_m = 0, t_b)$. So, the thickness function is given by

$$t_m(r) = \sqrt{r_m^2 + [t_b - z_m(r_m)]^2} \tag{4.25}$$

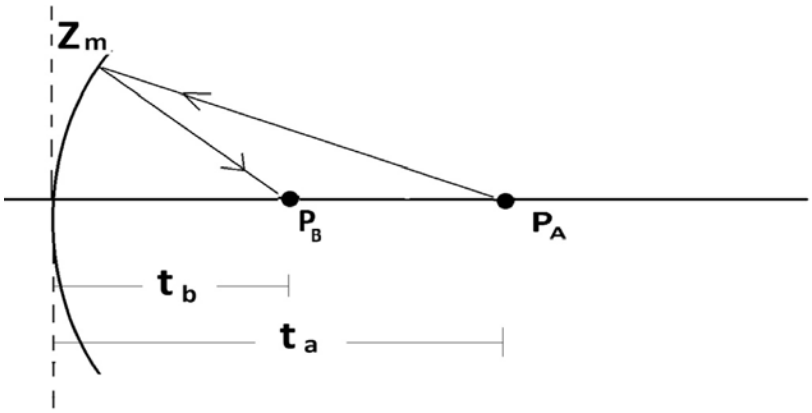

Figure 4.6: An concave mirror showing ray tracing. A coherent monochromatic light beam is reflected by surface z_m(r) to form an image located at back vertex distance tb. Point source P_A and image P_B positions are indicated.

After introducing the super-resolving surface $\tilde{z}_m(r_m)$, the thickness function is given by

$$\hat{t}_m(r) = \left\{ r_m^2 + [t_b - z_m(r_m) - \tilde{z}_m(r_m)]^2 \right\}^{\frac{1}{2}} \tag{4.26}$$

And again, the super-resolving mirror would be just described by

$$\hat{g}_m(r) = e^{ikt_{cm}} e^{ik\hat{t}_m(r)} \tag{4.27}$$

In order to choose the function $z_m(r)$, we must remember that there are some well-known optical configurations using mirrors where no spherical aberrations on axes are introduced, such as a concave spherical mirror with both its point object and point image on its radius of curvature, an ellipse with the image and object on their respective focuses, and a parabolic mirror with the point source at infinite and the image at its focus.

We show the results of our method using the last configurations; that is, using a parabolic mirror with $t_a = \infty$. For this example, as before, we will consider the following general parameters of design: light wavelength $\lambda = 633$ nm, $t_b = 40$ mm and a mirror diameter of 10 mm.

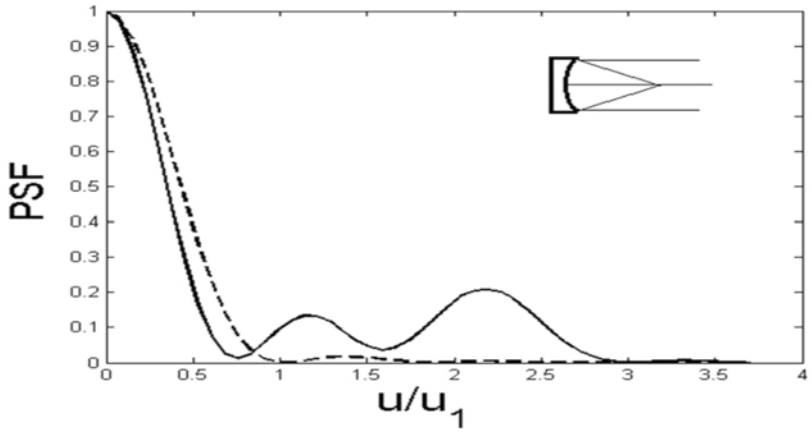

Figure 4.7: Normalized PSF of a mirror with its first surface given by a concave parabola. Dashed line represents the mirror ' s PSF with $z_m(r_m) = 0$.

Since the thickness formulas were already known, the procedure to calculate the PSF for the mirrors was quite similar to that used to calculate the PSF for the lenses; that is, following the four steps already mentioned in section 2, we obtained the super-resolving function

$$\tilde{z}_m(r) = -9.474[1 + \frac{cos(\frac{2.5\pi r}{a})}{k}] \tag{4.28}$$

The super-resolving PSF profile is shown in figure 4.7, where it can be observed a central core reduction of about 0.73, higher than the expected of 0.64. We also have obtained S=0.01. We attribute these unpredicted values to the off-axis aberrations introduced by the parabolic mirror [24]. So, the super-resolving PSF behavior is dependent of the aberrations mirror performance.

4.4 Design of a flat-aspheric lens

A flat-aspherical lens was designed taking all of the above into account. It was manufactured in the optical workshop at CIO. This was done in order to complement the theoretical part.

The parameters of the lens are:

Diameter = 100 mm
Central thickness = 20 mm
Focal distance = 700 mm
Aspherical Coefficient $A_2 = -1.361024e{-}3$
Aspherical Coefficient $A_4 = -1.056551e^{-9}$
Radius of the best Sphere = -368.2557 mm
Maximum deviation PV of best sphere=-2.84 μm

The wavefront of the lens was measured with the Wyko interferometer to demonstrate that it is designed at the diffraction limit. The laser, the interferometer and the sensor are located in Wyko case.

The basic operation of a Wyko interferometer is described below: a flat wave passes through a lens, then it reaches a mirror , which reflects the beam and passes through the lens again, later enter the Wyko case. This beam, called an object beam, interferes with the reference beam by generating interference fringes, which are collected in a sensor to finally be observed on a screen. The mirror is collocated at focal distance f. The Figure (4.8) shows an schematic of Wyko Interferometer and Figure(4.9) shows photos of Wyko Interferometer setup. Interference fringes have information about the aberrations of the measured lens. The mirror and other optical components of the Wyko have high optical quality so the aberrations of them are considered zero.

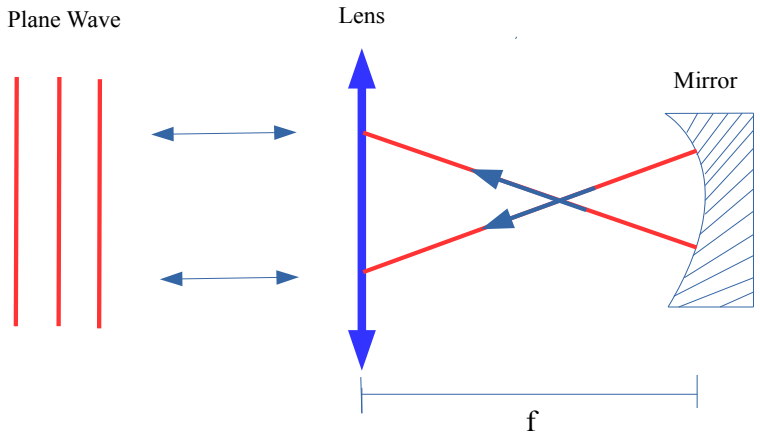

Figure 4.8: Schematic of Wyko Interferometer

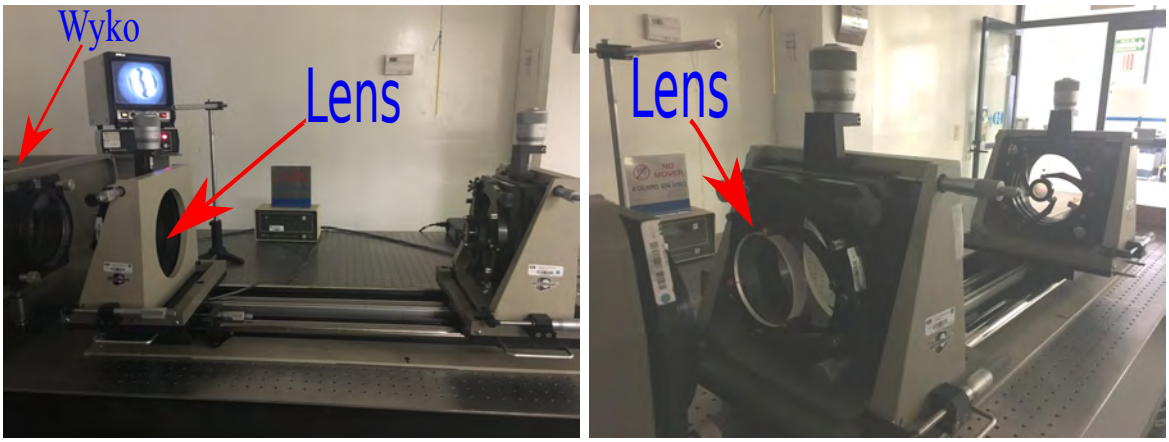

(a) (b)

Figure 4.9: Wyko Interferometer setup

The interferometer has software that measures several parameters related to the aberrations of the lens. The Figure (4.10) shows the wavefront of the lens. To consider that a lens is designed to the diffraction limit, the value of 20 Pt. PV must be less than or equal to a quarter of the length . 20 Pt PV represent the mean of 20 distances of Peak-valley of the wavefront [39]. The analysis results show that 20 Pt. PV value is 0.231 wv (wavelength), which means that it is designed at the diffraction limit.

Once the lens is designed to the diffraction boundary, a pupil will now be designed either of phase or of amplitude or both. We decided to work with a pupil of amplitude; so we made circles of different radius, whose center coincides with the center of the lens. This causes only a certain part of the beam to pass. The placement of these circles on the lens can be seen in Figure (4.11).

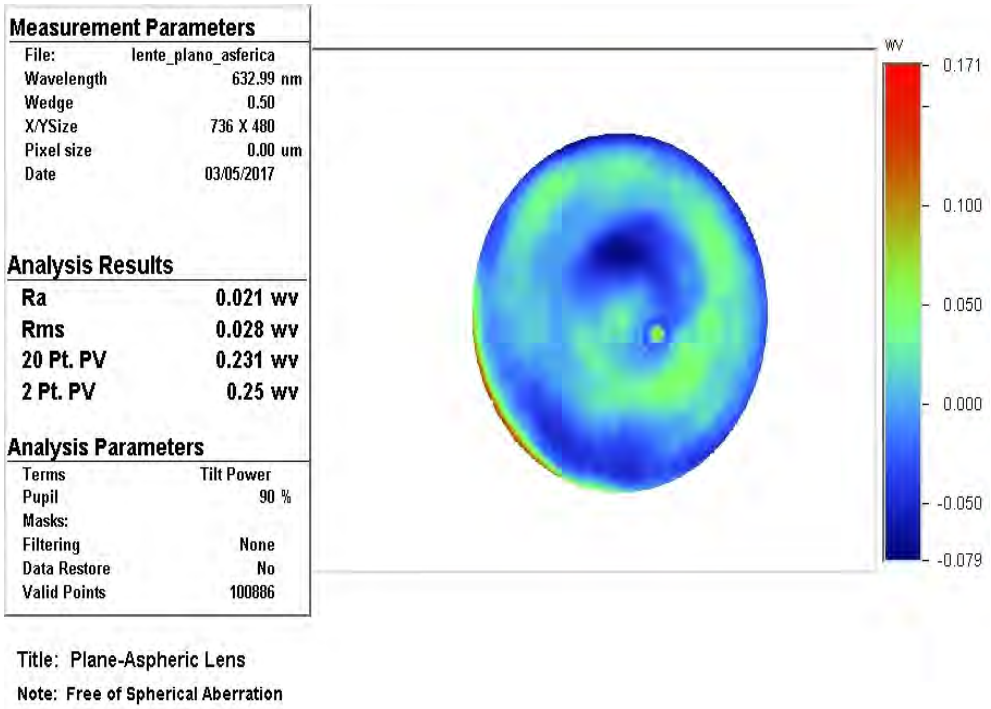

Figure 4.10: Wavefront of the flat-aspheric lens analyzed with Wyko interferometer.

Figure 4.11: Circles acting as amplitude pupils placed on the lens.

Now, we measure the different PSF's generated by the different pupils on lens. The optical setup to measure PSF can be observed in the Figure (4.12). A plane wave passes through the lens, then it falls on a microscope objective, which is located at the focal length of the lens. Finally it reaches the camera, which is connected to a pc. We obtain the images of the PSF's by using PC.

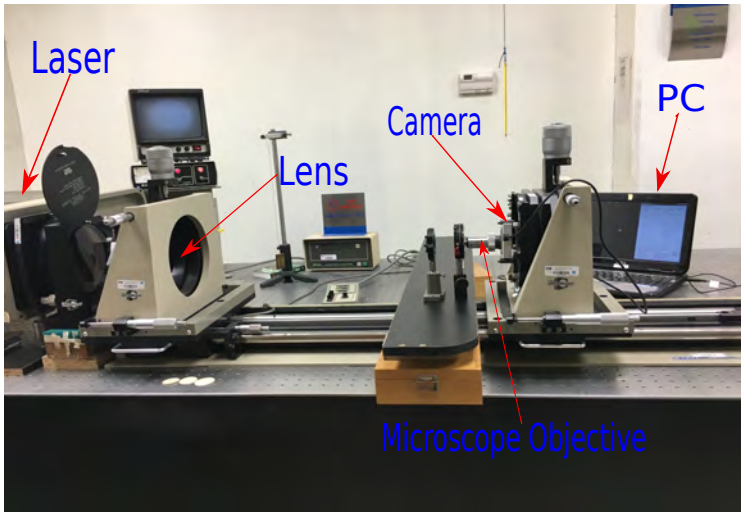

Figure 4.12: Optical setup to measure PSF.

Figure (4.13) shows PSF of a free pupil and PSF of an amplitude pupil. It can observed that the PSF is reduced by using an amplitude pupil. The values of the central line of the PSF's of Figure (4.13) are plotted for comparison purposes. The graphics are presented in Figure (4.14).

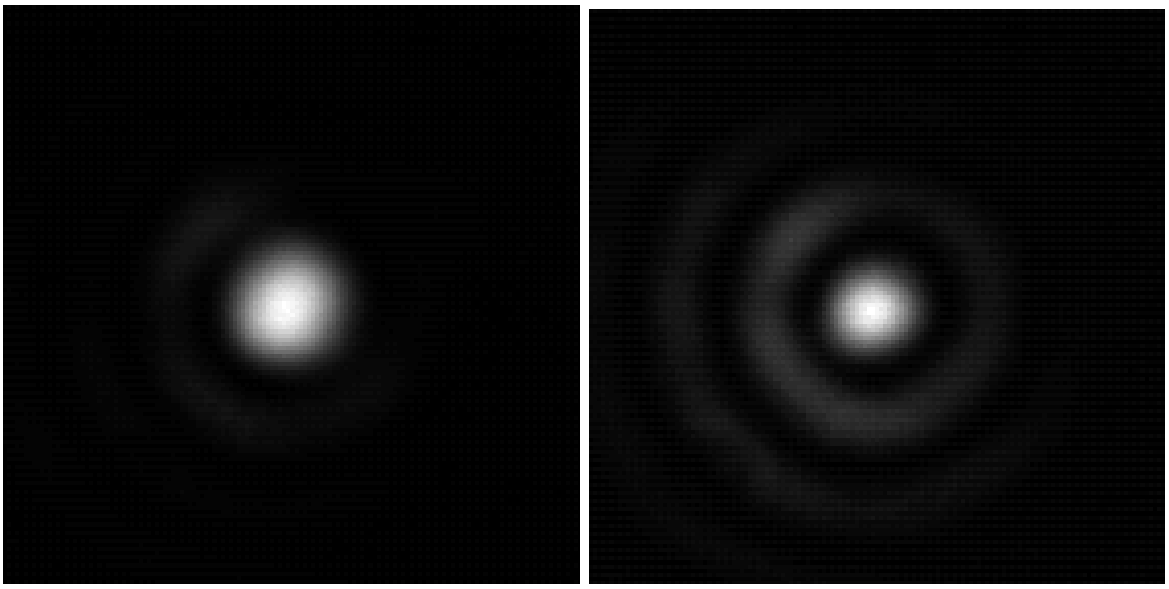

(a) (b)

Figure 4.13: a) PSF of a free pupil and b) PSF of an amplitude pupil

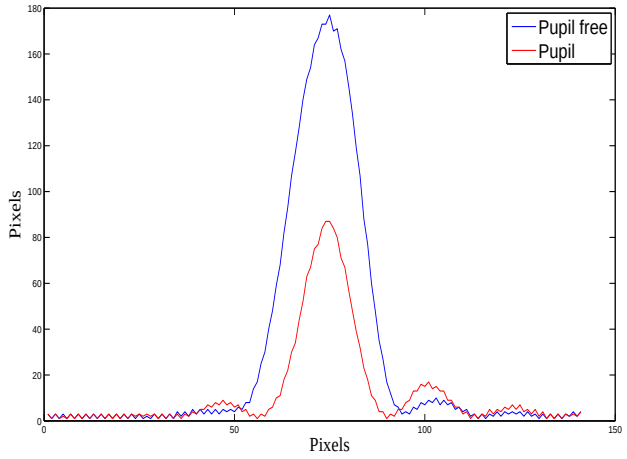

Figure 4.14: Comparison between PSF of free pupil and PSF of amplitude pupil

4.5 Discussion

Although it is rather obvious, we may think that a super-resolving function obtained for a particular design may be useful for other designs. In general, this situation will not occur. In Figure (4.15), we show the PSF's profiles of plano-hyperboloid lenses for different diameters and equal f-numbers. Using the same super-resolving function, designed for the

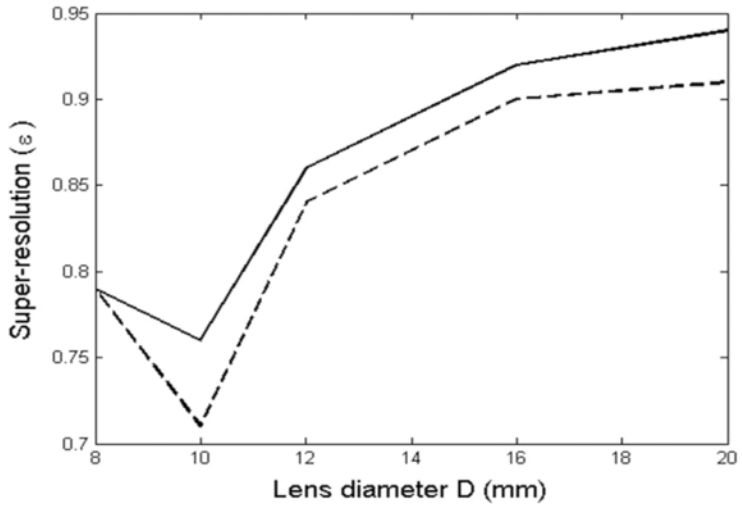

Figure 4.15: Relation between the super-resolution reduction factor ϵ and its diameter for various f/4 lenses. The super-resolving function was the same for all lenses and given by Equation(4.18). Continuous and dashed lines represent the results of analyzing the PSFs on-axis and out-of-axis, respectively.

lower lens diameter, it is observed that the PSF's super-resolution is gradually reduced until it vanishes. We have also observed this phenomenon with the super-resolving mirrors. So, the super-resolving functions depend on the mirrors and lens aperture values, and must be designed for each particular case.

We must say that the PSF's shown in this work were analyzed at its best focuses; hence the values of t_b used in Equation (4.7) differed slightly from those used in their respective geometrical designs. We found those focal shifts using Equation (4.7) to evaluate the on-axis intensity for a range of values of t_b.

When dealing with image formation it is important to know the out-of-axis behavior of the super-resolving PSF's. So, we will present some results using the biconvex lens of section 4.2.1. After determining the two thickness functions corresponding to those with and without the super-resolving function, we use Equation (4.7) to evaluate their respective PSFs. We choose $e(x, y)$ to describe a tilted flat wave along the x-direction (this way our PSF tilts along the u-direction). Figure (4.16) shows the PSFs in two positions: $u \approx 100u1 \approx 150\mu m$ and $u \approx 400u1 \approx 600\mu m$, where as mentioned before, $u_1 = 0.61\lambda f/D$. It can be appreciated that Figure (4.16 (a)) is almost a replica of Figure (4.3), that is, it is quite similar to its on-axis PSF; however in Figure (4.16 (b)), it is clearly seen the effects of the out-off-axis aberrations like coma and astigmatism. For the PSF without the super-resolving pupil the central core is increased and becomes assymetric. On the other

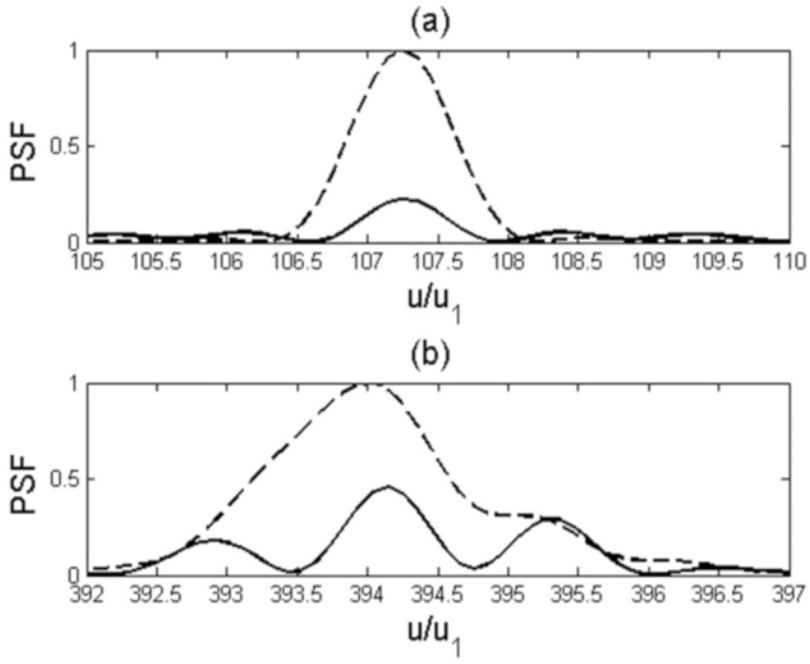

Figure 4.16: Out-off-axis PSFs of the biconvex lens of Section 4.2.1 calculated at two distances from axis: (a) 100 u_1 and (b) 400 u_1. u_1 is the first zero position of the non super-resolving PSF on axis. Continuous and dashed lines correspond to lens with and without super-resolving function, respectively.

hand, the PSF corresponding to the super-resolving lens the central core remains almost unaffected but the side lobes increases their height respect to the central one; that is, their Ω value are reduced when the PSF distance respect to the optical axis is increased. In this way we can determine the optimus image height were the super-resolution is maintained just by measuring the u-value were the respective value of Gamma achieves certain threshold value. In our example $u \approx 140u_1 \approx 210\mu m$, give us $\Omega = 4$, our defined threshold value.

Let us talk a little about the Schwarzchild representation of function $z_b(r) + \tilde{z}_b(r)$. Once having the polynomial representation of the super-resolving surface, for fabrication purposes, it would be convenient to write it like Equation (4.4). It is an easy task to do it by using a non-linear fitting. Just give the initial values like

$$C_{b=2B_2} \tag{4.29}$$

$$K_b = -1 + \frac{B_4}{B_2^3} \tag{4.30}$$

where B_j are the coefficients given by Equation (4.16). These initial values are the approximation to the curvature and conic constant obtained from the Taylor expansion of the radical function of Equation (4.4). In general, we suggest using the polynomial representation instead of that of Schwarzchild, since we found various super-resolving sags that cannot be represented accurately with the latter, especially for big aperture optics. We believe that this is not a serious limitation, since for fabrication purposes there are various polishing machines of aspherics that accept polynomial representations, for example [40].

Another important aspect of our proposal is related with the fabrication tolerances. If they are too tight, the fabrication of the super-resolving lenses will be difficult. In order to study this topic, we give the super-resolving sag of Equation (4.17) a fabrication error of 5%; that is, if we used $\tilde{z}_b(r) = (1 + 0.05)\tilde{z}_b(r)$ instead of $\tilde{z}_b(r)$, after evaluating the respective PSFs, we found that this sag error introduces only a slight change of the spot reduction of about 3%. So, the resulting lens with the errors would be super-resolving again (Figure (4.17)). The tolerances are an interesting topic that may help to find super-resolving pupils with better tolerances to fabrication errors.

Focusing efficiency and side lobe height are important aspects of superresolution. In this work we have fixed a side lobe eight of 0.2 ($\Omega = 5$) and left unconstrained the Strehl ratio S, our measure of the focusing efficiency, since we were more interested in controlling the spot reduction and the side lobes control, however, such constraint can be introduced in Equation (4.11). With our designs we have obtained S around 0.2, with means an efficiency around 20%, which is acceptable. Constraining Ω to higher values will render in higher image quality and less image artifacts. With the superresolving pupil defined by Equation (4.8) we can achieve higher values of Ω but ϵ increases as well, which is undesirable. So, in order to get the adequate balance among them, better optimization algorithms, to achieve global solutions, could be used [28], or use indirect techniques like those reported in [41].

As a final remark we must emphasize that in this report we have optimized a super-resolving sag given by Equation (4.12). In such equation is involved the refractive index, and inherently, we have assumed that such refractive index was equal to that of the lens; however, our analysis is not limited to this restriction. We can use a different refractive index to design the adequate thickness function, and with a different technique, add it to the lens. This means that we can use existing lens designs to convert them into super-resolving lens. Moreover, we have analyzed aspheric lenses and mirrors but our method could be used

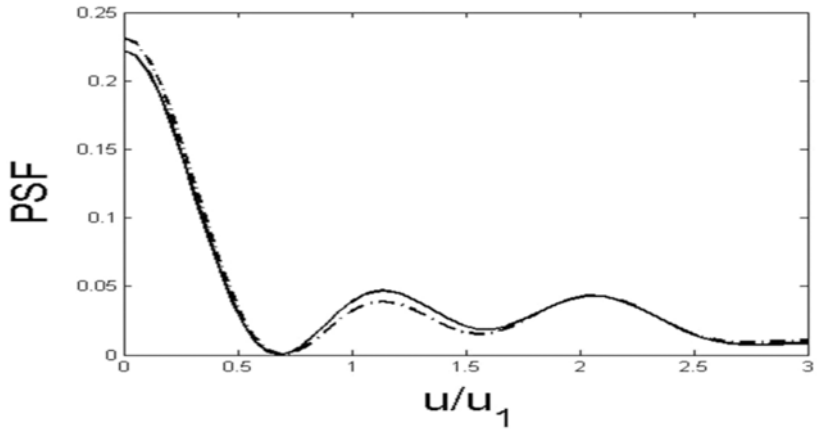

Figure 4.17: PSF modification due to lens fabrication errors.

to introduce super-resolution into other optical systems providing its thickness functions.

It has been demonstrated in this work that it is possible to design super-resolving lenses using smooth deformation functions and that the deformation functions can be polishable with fabrication tolerances not too tight. However, it still remains the challenge of fabricate such lens. The use of binary phase plates for achieving reduction of the central spot have been used in the past [42] and could be another alternative to smooth functions, how- ever, its incorporation to the lenses and mirrors would be the theme of future researches.

4.6 Conclusions

We have demonstrated that singlet lenses and mirrors can achieve super-resolution by adding deformation functions. It is reported that in general the super-resolving functions are dependent of the lens aperture. We developed analytical expressions and a design procedure that can help the fabrication of super-resolving lenses. Fabrication tolerances and out-off-axis analysis have been outlined. We expect that the combination of super-resolving lenses and super-resolving mirrors provide optical instruments with superior imaging characteristics.

We designed a lens to prove the theoretical method to obtain super-resolving lenses. We demonstrated that amplitude pupils reduce PSF.

Chapter 5

Paraboloid-aspheric lenses free of spherical aberration

Many researchers have used paraboloid lenses in their inventions [43]-[44]. For example, Hutchins [44] used a paraboloid lens to collect the light of a fiber-bundle. Paraboloid lenses have been used extensively to design tunable liquid lenses with thin elastic membranes or plates [45]-[46] and with tunable free surfaces manipulated by electrostatic fields [47]. Also, it is important to remember that paraboloid lenses have been designed in the opthalmic industry, specifically for spectacle lenses [48], hard and soft contact lenses [49]-[50] and intra-ocular lenses (IOLs) [51]. Note that the back surface of the eye´s lens, according to the Navarro´s simplified eye model as described by Gross et al. [52], is parab oloid. Paraboloid lenses have been used to solve specific problems in high-power optics as pulse formers for femto-second lasers [53], and these have been used for X- ray imaging [54]-[55]. All the paraboloid lenses above have spherical aberrations.

Technological advances make it possible to manufacture lenses with high surface qualities (resolution near to one Ångström: 1 Å= 0.1 (nm)) [56]. It is possible to make lenses with paraboloid surfaces using gravity [57]. These lenses can be adapted to several portable devices with cameras, such as smartphones and tablets. They can be converted to low-magnification portable microscopes.

In this work we describe the second surface of a lens, which corrects all spherical aberrations introduced by the first paraboloid surface, thus obtaining a perfect image of an object point situated on the optical axis. The first surface of the lens has a parabolic meridional section, which is described in a cylindrical-coordinate $(r, z(r))$ system with the same notation used in [37]. In other words, we determined the geometric profile of the second surface $z_b(r)$ for any given first preset paraboloid surface $z_a(r) = r^2/(4f_a)$, where f_a is the front vertex-focus distance of the paraboloid (and it corresponds to the focal distance of

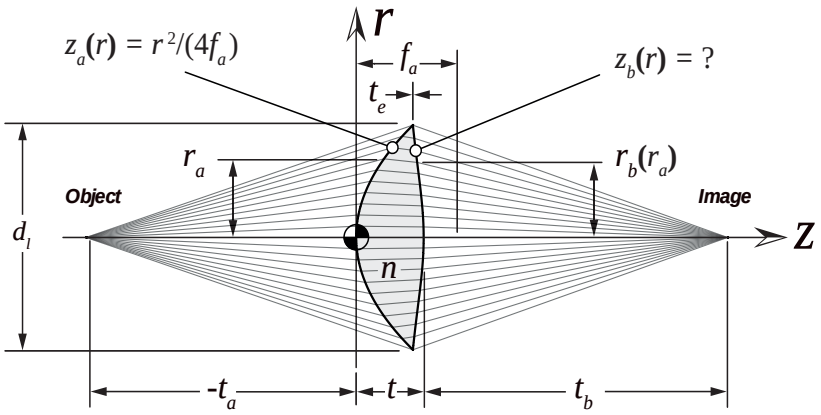

Figure 5.1: Design of positive paraboloid-aspheric lenses free of all orders of spherical aberration.

a paraboloid mirror with the same surface), shown in Figure (5.1). The Figure (5.1) is a design prescribed with a relative refractive index n, the first paraboloid surface $z_a(r)$ with focal distance f_a, an edge thickness t_e, a vertex anterior-object distance) t_a, a vertex-image point distance t_b, and a maximal-aperture diameter d_l. Center thickness t is calculated (in this example with $t_e = 0$). The main purpose of this work is to know the geometry of the second surface. A left-to-right ray tracing convention is used. A gaussian sign rule is assumed. It is important to mention that the maximal aperture can be bounded by the tangential marginal rays when the object is real and near the front vertex. The procedure will be described in the next section.

The first lenses free of spherical aberration, particularly bi-conical aspheric lenses and some kinds of spheric-oval or oval-spheric lenses, were studied by Descartes [22]. These rotational symmetrical lenses do not introduce spherical aberration in their interfaces separating isotropic and homogeneous mediums. In 1944, Luneburg [58] established the foundations in order to design aspheric-flat lenses for an object located at a finite distance, avoiding spherical aberration and using trigonometry to create parametric solutions. Also, he described spherical-aspheric lenses for an object at infinity to image a focal point on the optical axes without spherical aberration. With his classroom notes [58], Wasserman [59] and Wolf [3] propose a famous problem, well known as the 'Wasserman-Wolf problem', giving a numerical solution of a differential equation to determine the geometry of the last surface of an optical system to correct all spherical aberrations introduced by previous interfaces.

It is also important to highlight the work done by Stavroudis [60] and Shealy et al. [61]-[62], who tried to find the general analytical solution of the eikonal equation (they only managed to find the analytical solution of a corrective surface for certain non-paraboloid

cases), which ensures that rays are always perpendicular to the wavefronts, to determine, by means of vectorial, algebraic and differential methods, the last refracting surface of a lens system that generates a spherical wavefront in order to form an image on optical axis free of spherical aberration. Valencia et al. [37] managed to solve the eikonal problem for a single isotropic and homogeneous lens that is immersed in a medium that is also isotropic and homogeneous; they used algebraic artifices instead of numerical methods for the sake of accuracy. For this paper, we used Valencia's work to characterize the corrector surface of the spherical aberration introduced by a first paraboloid surface.

Many authors have studied the spherical aberration ([23],[63], [64],[65],[66],[2]) enhancing the image on an optical axis. With this work, many practical applications have appeared on the market, as singlet lenses for lithography, laser fusion, data storage and readout of optical disks ([67],[68],[69]).

In 2012, Valencia et al. [70] developed an analytical method to solve the Wasserman-Wolf problem for any kind of optical system composed of a single lens, with parametric and explicit solutions using the Schwarzchild´s approximations. They show the general procedure to find the analytical rigorous solution, and they show practical solutions to design flat-aspheric and spherical-aspheric lenses. But until now, nobody has described a bi-aspheric lens with a corrective surface for all orders of spherical aberration, keeping in mind that an aspherical surface is a non-spherical surface (where the prefix 'a-' indicates absence of sphericity). Every conical surface of revolution is aspheric, and thus, a paraboloid of revolution is an aspheric surface with a conical constant $K = -1$.

5.1 The exact aspheric corrective surface

The first surface with subindex a corresponds to a revolution paraboloid with a meridional section, which can be represented as

$$z_a(r_a) = \frac{r_a^2}{4f_a} = \frac{c_a r_a^2}{2} = \frac{c_a r_a^2}{1 + \sqrt{1 - (1 + K_a)\, c_a^2 r_a^2}}\,, \tag{5.1}$$

with a curvature at vertex $c_a = 1/(2f_a)$ and a conical constant $K_a = -1$ using Schwarzchild´s representation, well described by Malacara[2].

The derivative of the meridional function Equation (5.1) was calculated following the Valencia´s method[37]:

$$\frac{dz_a(r_a)}{dr_a} = \frac{r_a}{2f_a} = c_a\, r_a\,, \tag{5.2}$$

to calculate the odd abscissa $r_b(r_a)$ of a refracted ray at the posterior aspheric surface with

$$r_b(r_a) = \frac{B^2FG - s_4OP + s_5\ \mathrm{sign}(r_a)\, B\sqrt{(FP - s_4OG)^2 + K(P^2 - B^2G^2)}}{B^2(F^2 + K) - O^2}\Big|_{r_a}, \tag{5.3}$$

and the even ordinate $z_b(r_a)$ with

$$z_b(r_a) = \left[\frac{1}{2}c_a r_a^2 + D\,(r_a - r_b(r_a)) + s_1\,E\,|r_a - r_b(r_a)|\right]\Big|_{r_a}, \tag{5.4}$$

where the absolute value is a safeguard to protect the lens maker, with recursive variables B, D, E, F, G, K, O, and P. Note that the recursive variables are functions of parameter r_a, which corresponds to the height of the input ray. For this reason, the notation of evaluation $|_{r_a}$ is used to indicate that the recursive variables are parametric functions.

The method presented here to design singlet lenses free from all orders of spherical aberration is an application of the method used in [37]. Thus, the general solution was slightly modified to reduce the number of recurrent variables required for Equations (5.3) and (5.4).

$$
\left.
\begin{aligned}
B =& \sqrt{r_a^2(c_a^2\, r_a^2 - 2\, c_a t_a + 2)^2}\,, \\
D =& \frac{n^2 c_a[(c_a r_a^2 - 2\, t_a)^2 + 4\, r_a^2]}{r_a\,(c_a\{c_a(n^2-1)[(c_a r_a^2 - 2\, t_a)^2 + 4\, r_a^2] + 8\, t_a\} - 4)}\,, \\
E =& \frac{\sqrt{(c_a^2 r_a^2 - 2\, c_a t_a + 2)^2}}{\sqrt{r_a^2}} \\
& \times \frac{\sqrt{n^2(c_a^2 r_a^2 + 1)[(c_a r_a^2 - 2\, t_a)^2 + 4\, r_a^2] - r_a^2(c_a^2 r_a^2 - 2\, c_a t_a + 2)^2}}{c_a\{c_a(n^2-1)[(c_a r_a^2 - 2\, t_a)^2 + 4\, r_a^2] + 8\, t_a\} - 4}\,, \\
F =& n^2\sqrt{(c_a r_a^2 - 2\, t_a)^2 + 4\, r_a^2}\,, \\
G =& \frac{r_a}{2}(n^2[c_a^2 r_a^2 - 2\, c_a(t + t_b) + 2]\sqrt{(c_a r_a^2 - 2\, t_a)^2 + 4\, r_a^2} + s_2\,\sqrt{(c_a^2 r_a^2 - 2\, c_a t_a + 2)^2} \\
& \times \left[2(-t_a + nt + t_b) + \mathrm{sign}(t_a)\sqrt{(c_a r_a^2 - 2\, t_a)^2 + 4\, r_a^2}\right])\,, \\
K =& r_a^2(c_a\{(n^4-1)c_a[(c_a r_a^2 - 2\, t_a)^2 + 4\, r_a^2] + 8\, t_a\ \} - 4)\,, \\
O =& r_a(s_4\left(\frac{n^2(n^2-1)c_a[(c_a r_a^2 - 2\, t_a)^2 + 4\, r_a^2]\,(c_a^2 r_a^2 - 2\, c_a t_a + 2)^2}{c_a\{(n^2-1)c_a[(c_a\, r_a^2 - 2\, t_a)^2 + 4\, r_a^2] + 8\, t_a\} - 4}\right) + s_1 \\
& \times\sqrt{(c_a^2 r_a^2 - 2\, c_a t_a + 2)^2}\left(\frac{c_a\{(n^4-1)c_a[(c_a r_a^2 - 2\, t_a)^2 + 4\, r_a^2] + 8\, t_a\} - 4}{c_a\{(n^2-1)c_a[(c_a r_a^2 - 2t_a)^2 + 4\, r_a^2] + 8\, t_a\} - 4}\right) \\
& \times\sqrt{n^2(c_a^2 r_a^2 + 1)[(c_a r_a^2 - 2\, t_a)^2 + 4\, r_a^2] - r_a^2(c_a^2\, r_a^2 - 2\, c_a t_a + 2)^2})\,, \\
P =& r_a^2(\left(\frac{c_a\{(n^4-1)c_a[(c_a r_a^2 - 2\, t_a)^2 + 4\, r_a^2] + 8\, t_a\} - 4}{c_a\{(n^2-1)c_a[(c_a r_a^2 - 2\, t_a)^2 + 4\, r_a^2] + 8\, t_a\} - 4}\right)\{n^2 c_a[(c_a r_a^2 - 2\, t_a)^2 + 4\, r_a^2] \\
& + s_1\, s_4\,\sqrt{n^2(c_a^2 r_a^2 + 1)[(c_a r_a^2 - 2\, t_a)^2 + 4\, r_a^2] - r_a^2(c_a^2 r_a^2 - 2\, c_a t_a + 2)^2} \\
& \times\sqrt{(c_a^2 r_a^2 - 2\, c_a t_a + 2)^2}\} - \tfrac{1}{2}\{2n^4 c_a[(c_a r_a^2 - 2\, t_a)^2 + 4\, r_a^2] + (c_a^2 r_a^2 - 2\, c_a t_a + 2)^2 \\
& \times[c_a r_a^2 - 2(t + t_b)] + s_2\, n^2\, c_a\sqrt{(c_a^2 r_a^2 - 2\, c_a t_a + 2)^2} \\
& \times\{2(-t_a + nt + t_b)\sqrt{(c_a r_a^2 - 2\, t_a)^2 + 4\, r_a^2} + \mathrm{sign}(t_a)\,[(c_a r_a^2 - 2\, t_a)^2 + 4\, r_a^2]\})\},
\end{aligned}
\right\} \qquad (5.5)
$$

and unknown dichotomic sign functions s_1, s_2, s_4 and s_5 .

The above solution Equations (5.3)-(5.5), with the rules for each sign found by means of numerical analysis, can be resumed using a new system of lowercase recurrent variables (that are functions of the parameter r_a) to improve and speed up the computing process:

$$
r_b(r_a) = \frac{r_a(f\, m\, p - \hat{t}\, u + \hat{s}_5\,\mathrm{sign}(t_b)\, e\,\sqrt{(m\, u - \hat{t}\, p)^2 + c\, q(u^2 - f\, p^2)})}{f(m^2 + c\, q) - \hat{t}^2}\Big|_{r_a}\,, \qquad (5.6)
$$

$$z_b(r_a) = \frac{c_a c}{2} + \frac{a\,k(1 - r_b/r_a) + \hat{s}_1 \,\mathrm{sign}\,(t_a)\, e\sqrt{a(d+1)h - cf}\,\sqrt{(1 - r_b/r_a)^2}}{\hat{r}}\Big|_{r_a}\,, \tag{5.7}$$

with the following recurrent variables in lower case:

$$\left.\begin{aligned}
a &= n^2\,,\\
b &= a - 1\,,\\
c &= r_a^2\,,\\
d &= c_a^2\, c\,,\\
e &= -d + 2(c_a\, t_a - 1)\,,\\
f &= e^2\,,\\
g &= \sqrt{(c_a\, c - 2t_a)^2 + 4c}\,,\\
h &= g^2\,,\\
k &= c_a\, h\,,\\
l &= b\, k\,,\\
m &= a\, g\,,\\
o &= e[\mathrm{sign}(t_a)(n\, t + t_b - t_a) + g/2]\,,\\
p &= [d/2 - c_a\,(t + t_b) + 1]\, m + o\,,\\
q &= c_a\,[(a+1)\, l + 8t_a] - 4\,,\\
\hat{r} &= c_a\,(l + 8t_a) - 4\,,\\
s &= \mathrm{sign}(t_a)\, q\, e\sqrt{a\,(d+1)\, h - c\, f}\,,\\
\hat{t} &= \frac{a\, l\, f + s}{\hat{r}}\,,\\
u &= \frac{a\, k\, q + s}{\hat{r}} - [a^2 k + \frac{f}{2}(c_a\, c - 2(t + t_b)) + a\, c_a\, g\, o]\,,
\end{aligned}\right\} \tag{5.8}$$

with the following rules for only two signs ($\hat{s}_1$ and $\hat{s}_5$) included in the general solution Equations (5.6)-(5.7):

$$
\left.
\begin{array}{ll}
\hat{p} = & r_a^2 + \dfrac{2}{c_a^2} - \dfrac{2t_a}{c_a} - \dfrac{2n\sqrt{(n^2-1)(1-2c_at_a)}}{c_a^2\,(n^2-1)}\,, \\
\hat{q} = & r_a^2 + \dfrac{2}{c_a^2} - \dfrac{2t_a}{c_a} - \dfrac{2n^2\sqrt{(n^4-1)(1-2c_at_a)}}{c_a^2\,(n^4-1)}\,, \\
\hat{v} = & r_a^2 - 4f\,t_a + 8f^2\,. \\
\hat{s}_1 = & 1\,, \\
\hat{s}_5 = & \mathrm{sign}(\hat{v})\,. \\
\textbf{If} & t_a > -2\,f_a/(n-1) \ \textbf{and} \ t_a < 0\,, \\
\textbf{then} & \hat{s}_1 = \mathrm{sign}\,(\hat{p})\,; \ \ \hat{s}_5 = \mathrm{sign}\,(\hat{p})\ \mathrm{sign}\,(\hat{q})\ \mathrm{sign}\,(\hat{v}) \\
\textbf{End If}\,. & \\
\textbf{If} & t_a >= 0 \ \textbf{and} \ t_a <= 2\,f_a/(n^2+1)\,, \\
\textbf{then} & \hat{s}_5 = \mathrm{sign}\,(\hat{q})\ \mathrm{sign}\,(\hat{v}) \\
\textbf{End If}\,. &
\end{array}
\right\} \qquad (5.9)
$$

The rule of signs (Equation (5.9)) ensures the continuity of corrective surfaces. With this rule invalid solutions are never presented. The final solution is infinitely differentiable with respect to parameter r_a. The solutions Equations (5.6)-(5.8) always are reals using the rule signs, Equation (5.9).

5.2 Different cases of design of thick lens with object and image at finite distances

We show some results obtained for a front convex paraboloid surface ($f_a > 0$) whose sagitta is given by Equation (5.1). The internal rays of this solutions have no inversion. So, we present some examples of different cases of design of convex paraboloid-aspheric lens. In this section, Ob. represents object point and Im. is the image point.

The simplified general solution, for a first convex paraboloid surface with a proximal[1] or distant object and a proximal image, according to Equations (5.6)-(5.7) with the recurrent variables according to Equation (5.8) and signs Equation (5.9), was verified by means of ray tracing. Also, to verify the solution, the back vertex curvature of these paraboloid-aspheric lenses can be obtained by means of the Pinching Theorem described by Weisstein [71, 72], at the points of discontinuity when $t_a = -2\,f_a/(n-1)$, $t_a = 0$ and $t_a = 2\,f_a/(n^2+1)$ using Valencia's formulas with $R_a = 2\,f_a$:

[1]For Equations (5.6)-(5.8), to give ever valid results (regular surfaces), the anterior vertex-object distance t_a, of its five irregular values, should be of at least $1\,(nm)$, either above or below these four critical values, if the object is real when $t_a = -2\,f_a/(n-1)$ and $t_a = -2\,f_a/(n^2-1)$, or virtual when $t_a = 2\,f_a/(n^2+1)$ and $t_a = 2\,f_a/(n+1)$; when $t_a = 2\,f_a$, it should be below the critical point.

$$c_b(0) = \frac{\left.\dfrac{dz_b(r_a)}{dr_a}\right|_{r_a = 0}}{\left[\lim\limits_{r_a \to 0}\left(\dfrac{r_b(r_a)}{r_a}\right)\right]^2}, \tag{5.10}$$

$$c_b(0) = \frac{(n-1)(t + n\,t_b)\,t_a + 2\,f_a[t + n(t_b - t_a)]}{(n-1)\,t_b[2\,f_a(n\,t_a - t) - (n-1)\,t\,t_a]} = \frac{1}{R_b}, \tag{5.11}$$

a solution that corresponds to a Gaussian central back curvature radius [2]

$$R_b = \frac{(n-1)\,t_b[2\,f_a(n\,t_a - t) - (n-1)\,t\,t_a]}{(n-1)(t + n\,t_b)\,t_a + 2\,f_a[t + n(t_b - t_a)]}, \tag{5.12}$$

In order to guarantee that the Equation (5.6) and Equation (5.7) with recurrent variables (Equation (5.8)) and signs established in Equation (5.9) yield an optical design without spherical aberration, we proved them through ray tracing of a lot of designs. Figures (5.2-5.5) show some examples of each case respectively.

In Figure (5.2), aspherical back surfaces $z_b(r_a)$ were calculated using Equations (5.7) -(5.8) with the rules of Equation (5.9), in (a), (b), (c) and (d), to obtain image-points free of all orders of spherical aberration. Rays are traced with several prescribed variables: relative refraction index $n = 1.5$, front vertex radius $R_a = 2\,f_a = 50$ (mm), image distance $t_b = 100$ (mm), center thickness $t = 10$ (mm), and object distance $t_a = -1000$, -100, -50, and -25 (mm) for (a), (b), (c), and (d) respectively. The back aperture diameters $d_b =$ 50, 46.09753, 38.199538 and 30.358034 (mm) were preset for (a) and numerically calculated with
$d_b = d_l$ for (b), (c) and (d) respectively. Lens (a) diameter $d_l = 61.124557$ was calculated. Rays travel upwards. In this case, maximum lens diameter is bounded by $d_l \leq 2\sqrt{-f_a\,t_a}$.

In Figure (5.3), four lenses were prescribed with a relative refraction index $n = 1.7$, a front vertex radius of $R_a = 2\,f_a = 50$ (mm), a back vertex-image distance $t_b = 60$ (mm), a lens diameter $d_l = 30$ (mm), and a center thickness with $t = 5$ (mm). Object distances $t_a = 100$, 65, 25, and 6 (mm) were prescribed for (a), (b), (c), and (d) respectively. Aspherical back surfaces $z_b(r_a)$ to obtain zero spherical aberration were calculated using Equations (5.6)-(5.9). Edge thicknesses were calculated with $t_e = 4.169306, 5.236779$ and 13.306509 for (a), (b) and (c) respectively. Lens (d) has to be lenticular. Rays travel upwards. Two additional extended emergent rays are shown with phantom lines in each lens to indicate

[2] Using formulas for the axial lensmaker [37] with finite conjugate planes, valid for all lenses without quadrant inversion within the same (I and II Figure (5.1)).

the position of the virtual object-point O.

In Figure (5.4), designs can be negative or positive. Five lenses were prescribed with relative refraction index $n = 1.6$, front vertex radius $R_a = 2\,f_a = 70$ (mm), center thickness $t = 5$ (mm), back vertex-image distance $t_b = -50$ (mm), and front vertex-object distances $t_a = -120$, -80, -40, -25 and -12 (mm) for (a), (b), (c), (d) and (e) respectively. Lens diameter $d_l = 50$ (mm) was prescribed for (a), (b) and (c) with negative designs. Maximum diameters $d_l = 47.136995$ and 23.243589 (mm) for the positive designs (d) and (e) were calculated. Aspherical back surfaces $z_b(r_a)$ were calculated to obtain zero spherical aberration using Equations (5.6)-(5.9). Edge thicknesses were calculated with $t_e = 9.348011, 7.689600$ and 3.527993 for negative designs (a), (b) and (c) respectively. Rays travel upwards. Two additional extended incident rays are shown with phantom lines in each lens, to indicate the position of the virtual image-point $\boldsymbol{I}$. In this case, maximum lens diameter is bounded by $d_l \leq 2\sqrt{-f_a\,t_a}$.

In Figure (5.5), four lenses were prescribed with negative design, relative refraction index $n = 1.7$, front vertex radius $R_a = 2\,f_a = 60$ (mm), center thickness $t = 4$ (mm), diameter $d_l = 35$ (mm), back vertex-image distance $t_b = -60$ (mm), and front vertex-object distance $t_a = 65$, 40, 30 and 20 (mm) for (a), (b), (c) and (d) respectively. Aspherical back surfaces $z_b(r_a)$ were calculated to obtain zero spherical aberration using Equations (5.6)-(5.9). Edge thicknesses were calculated with $t_e = 11.829075, 16.418563$ and 29.630340 for negative designs (a), (b) and (c) respectively. Lens (d) has to be lenticular in order to avoid backward rays. Rays travel upwards. Four additional extended (incident and refracted) rays are shown with phantom lines in each lens to indicate the position of the virtual object-point O and the virtual image-point I.

5.2.1 Real Ob. - Real Im.

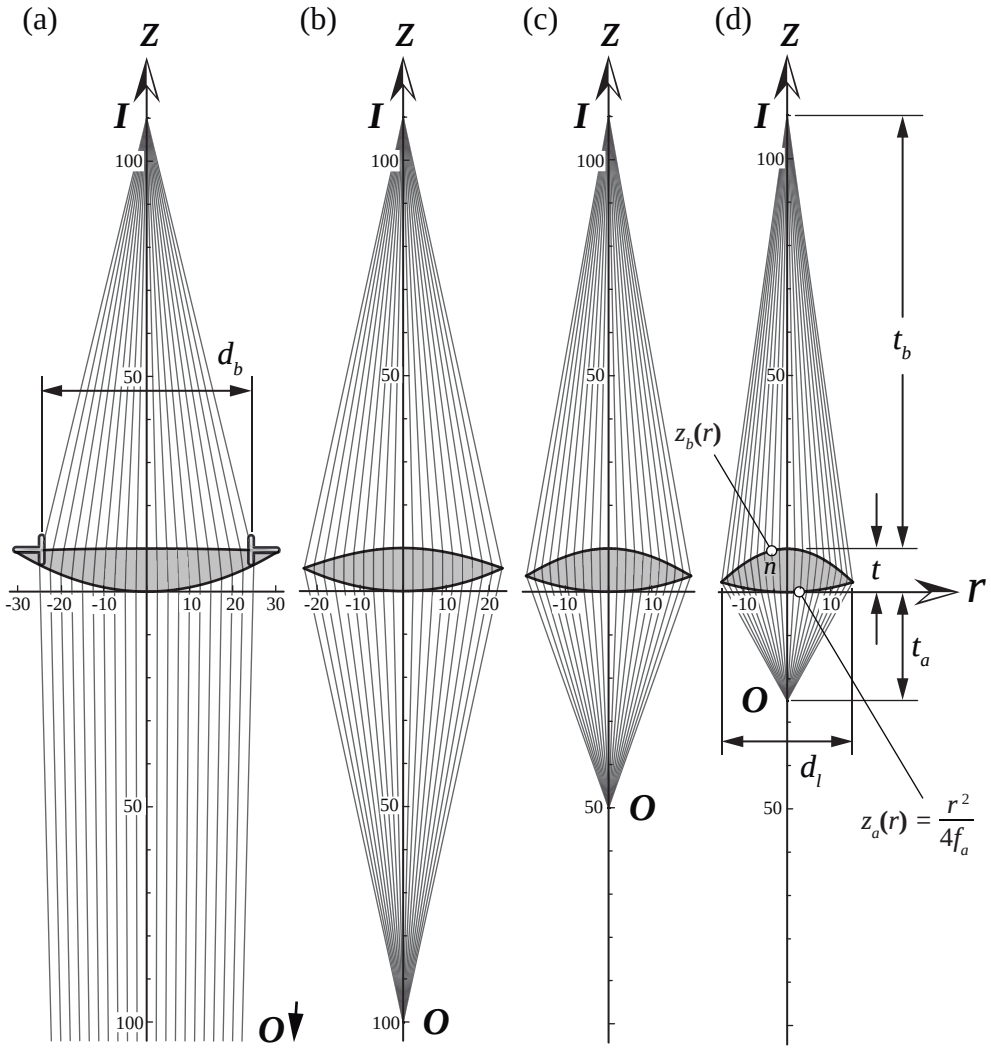

Figure 5.2: Positive design of paraboloid-aspherical biconvex lenses with zero spherical aberration, with several real objects O and the same real image I, maximum possible diameter d_l and null edge thicknesses $t_e = 0$.

5.2.2 Virtual Ob. - Real Im.

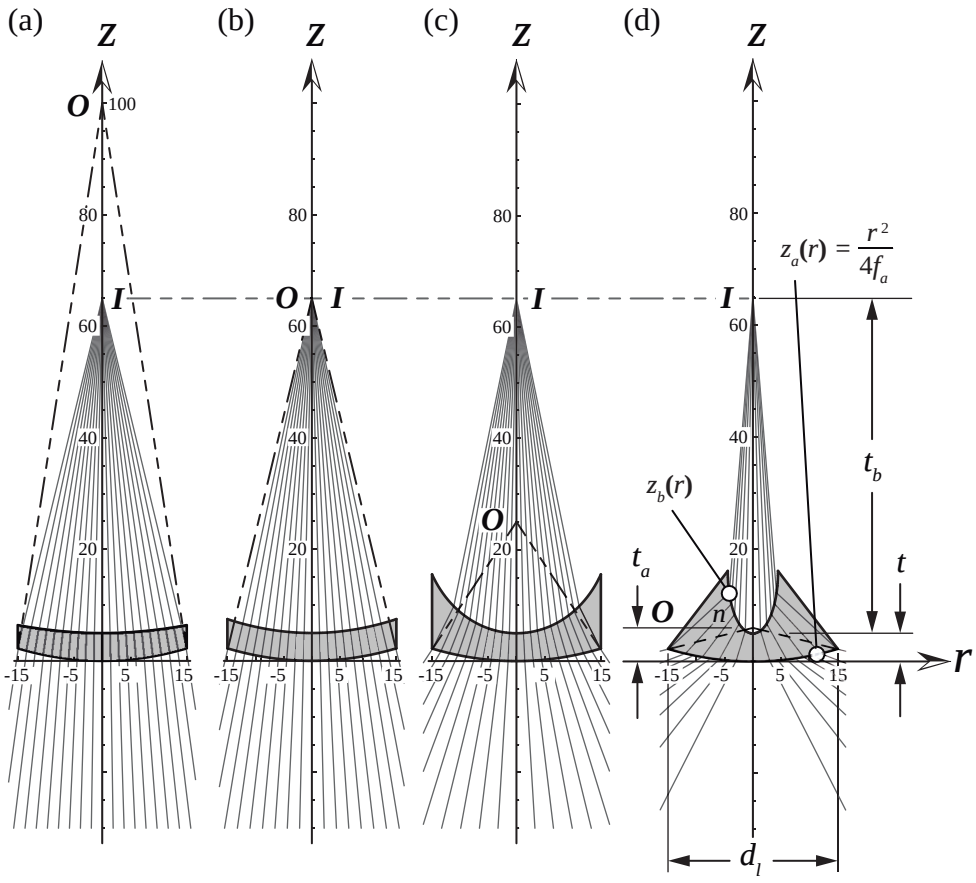

Figure 5.3: Positive or negative designs of paraboloid-aspherical convex-concave lenses featuring zero spherical aberration with a virtual object O and a real image I.

5.2.3 Real Ob. - Virtual Im.

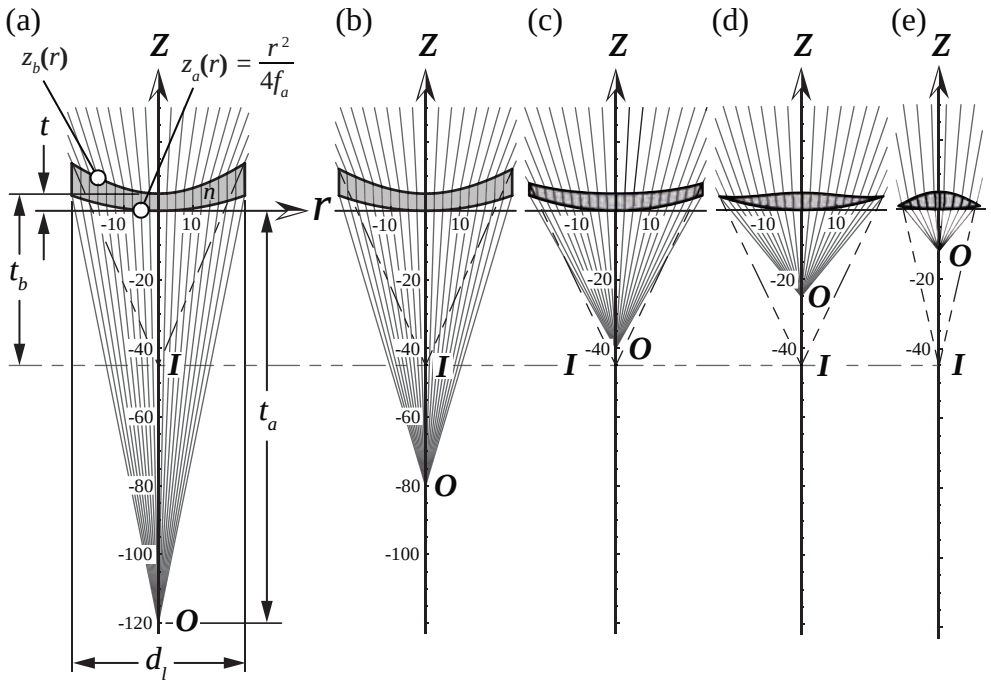

Figure 5.4: Paraboloid-aspherical convex-inflexed simple lenses with a real object O and a virtual image I.

5.2.4 Virtual Ob. - Virtual Im.

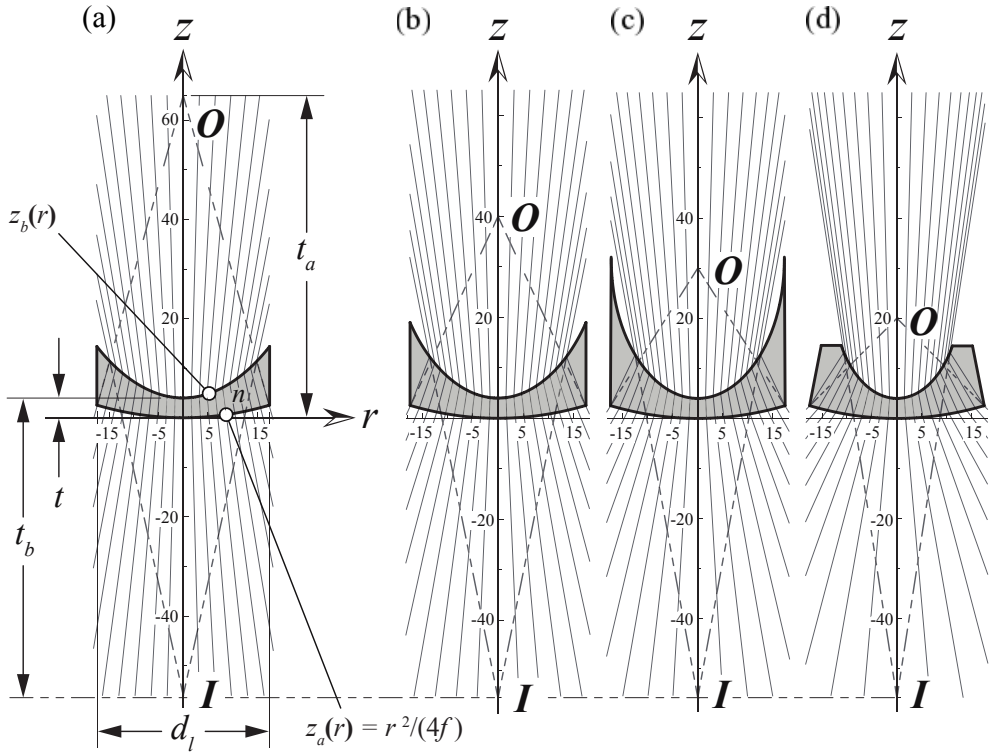

Figure 5.5: Paraboloid-aspherical convex-concave simple lenses with a virtual object O and a virtual image I.

5.3 An approximation of the formula of Schwarzschild with coefficients of deformation

In order to find solutions with Schwarzschild's formula with coefficients of deformation (ISO standard 10110-12), Valencia shows the general procedure in [37] . Thus, we used it. We consider that the first four aspheric coefficients are more important, so the sum of Equation (5.13) is finite.

In the other hand, to find the appropriate conic constant K_b (of the correcting surface) that determines the best fit when the result is dependent on the aperture diameter, we can begin with the numerical solution for K_b in

$$\sum_{j=2}^{5}\left[B_{2j}\left(\frac{d_b}{2}\right)^{2j}\right]=0, \tag{5.13}$$

or with a better solution that can be obtained through approximation using software, where d_b is the back aperture diameter, and $d_b \leq d_l$.

Once a suitable conic constant has been obtained, this can be iteratively optimized with very small changes of K_b to minimize the spherical aberration.

An example of the results obtained following Valencia's method, asphericity coefficients according ISO formula (which determine the best fit of the correcting surface of spherical aberration for a first paraboloid interface) for an object at infinity were obtained using Equations (5.6)-(5.7) with recurrent variables Equation (5.8) and signs Equation (5.9), and calculating their limits when t_a tends toward minus infinity, to obtain

$$B_{2j}=\frac{Q_{2j}}{m^j U^{\,3j-2}\,(\,2\,t_b)^{\,2j-1}}-(-1)^{\,j+1}\,c_b^{\,2j-1}\,(1+K_b)^{j-1}\mathrm{Bin}\left[\frac{1}{2},j\right] \tag{5.14}$$

with recursive variables $U=2\,n\,f_a-m\,t$ and $p=n+1$, and polynomials Q_{2j} that correspond to:

$$
\left.
\begin{aligned}
Q_4 &= p\,U^4 - m\,n\,t_b(m^3 p\,t\,t_b^2 + 2m\,t_b\,U^2 + 2U^3)\,,\\
Q_6 &= 2m^6\,n\,p^2 t\,t_b^5\,(2m\,t + U) + 2m\,n\,t_b\,U^2\{4m^4\,p\,t\,t_b^3 + m^3\,t_b^2\,[p\,(t + t_b) - 2U]\,U\\
&\quad -m\,(n-3)t_b\,U^3 + 3p\,U^4\} - 2p^2U^7\,,\\
Q_8 &= -2m^3 n\,t_b^3 U^6\{m[(5n-8)n+7]\,t_b - 2[n(n+7)-4]U\} + 4m^3 n\,p\,t_b^2 U^4\{m^3\\
&\quad \times(4n-11)t\,t_b^3 + m^2 t_b^2[(n-4)t_b - 6t]U + 5U^4\} + 2m\,n\,p^2 t_b\,U^2[-28m^7 t^2 t_b^5\\
&\quad -4m^6 t\,t_b^4\,(t + 5t_b)U - 2m^5 t_b^5\,U^2 - 3m^3 t\,t_b^2 U^4 - 10U^7] - p^3(24m^{10} n\,t^3 t_b^7\\
&\quad +24m^9 n\,t^2 t_b^7 U + 5m^8 n\,t\,t_b^7 U^2 - 5U^{10})\,,\\
Q_{10} &= 176m^{13} n\,p^4 t^4 t_b^9 + 264m^{12} n\,p^4 t^3 t_b^9 U + 4m^{11} n\,p^3 t^2 t_b^8(120t + 29p\,t_b)U^2 + 2m^{10}\\
&\quad \times n\,p^3 t\,t_b^7(24t^2 + 288t\,t_b + 7p\,t_b^2)U^3 - 16m^9 n\,p^2 t\,t_b^7[(6n-31)t - 11p\,t_b]U^4\\
&\quad +2m^8 n\,p^2 t_b^6[2(5n+42)t^2 - (41n-201)\,t\,t_b + 5p\,t_b^2]\,U^5 + 8m^7 n\,p\,t_b^5\{3p^2 t^2\\
&\quad +[3n(3n-4)+35]\,t\,t_b - (n-8)p\,t_b^2\}U^6 - 4m^6 n\,p\,t_b^5\{[n(6n+19)-43]t - [n\\
&\quad \times(3n-16)+23]t_b\}U^7 - 4m^5 n\,t_b^4(4(2n-5)p^2 t + \{n[n(7n-20)+9] - 20\}t_b)U^8\\
&\quad +4m^4 n\,t_b^3(5p^3 t + \{n[n(9n+19)-31]+15\}t_b)U^9 + 20m^3 n[n(2n-9)\\
&\quad +3]p\,t_b^3 U^{10} - 10m^2(11n-7)n\,p^2 t_b^2 U^{11} + 70m\,n\,p^3 t_b\,U^{12} - 14p^4 U^{13}\,.
\end{aligned}
\right\} \qquad (5.15)
$$

Figure (5.6) shows ray tracing for a paraboloid-aspherical lens with reduced spherical aberration, with deformation coefficients Equation (5.14). Figure (5.6 a) shows the ray tracing for the lens, obtained by OSLO® without optimization algorithm nor defocus. Aspherical back surface was calculated with an entrance beam radius of 25.2 (mm) that corresponds to output aperture (stop diameter) $d_d = 48.720006$ (mm), with back vertex radius $R_b = -141.463415$ (mm), conical constant $K_b = -7.84569$, and four coefficients $B_4 = 1.7315 \times 10^{-8}$ (mm^{-3}), $B_6 = 4.6923 \times 10^{-12}$ (mm^{-5}), $B_8 = -2.7666 \times 10^{-15}$ (mm^{-7}), and $B_{10} = 1.0514 \times 10^{-18}$ (mm^{-9}). Figure (5.6 b) shows the respective spot diagram (mm), also obtained without the optimization algorithm nor defocus.

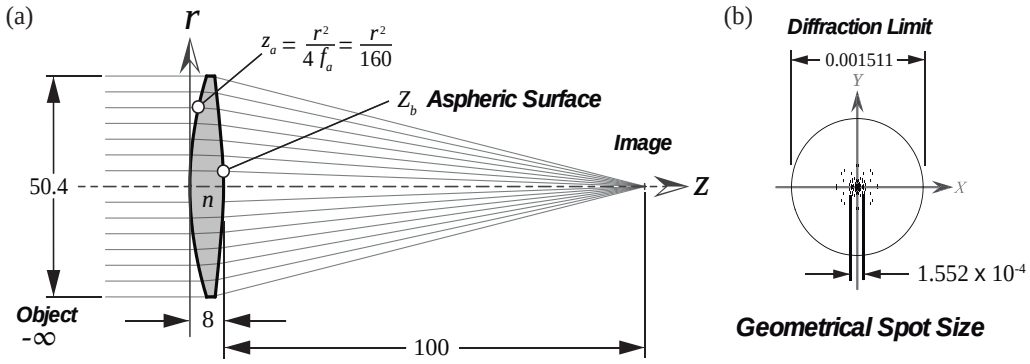

Figure 5.6: Paraboloid-aspherical lens with object at infinity and real image, with prescribed variables $n = 1.5$, $R_a = 2\ f_a = 80$ (mm), $t_a = -\infty$, $t = 8$ (mm), $t_b = 100$ (mm), lens diameter $d_l = 50.4$ (mm), and working $F\# = 2.052545$.

5.4 Conclusion

We have presented the analytical equations to design singlet lens with a paraboloid convex surface without spherical aberration. Since for optical designers it is convenient to use the Schwarzchild's formula with coefficients of deformation, we present the corresponding approximation for the described lenses for an object placed at infinity. The aspheric coefficients are shown as well.

The formulas used in [37] were applied in the case in which the lens has a first convex spherical surface; in this paper, we consider a first-convex paraboloid surface. It is worth noting that the formulas presented for concave cases are exactly alike. Besides, the general method presented in [37] applies to many kinds of singlet lenses, but the deductive process to obtain the rigorous or approximate solution of the corrective aspheric surface, which is ISO-compliant, is specific for each kind of lens, and it also aids in analytically determining the coefficients of deformation.

The exact parametric solutions allow designs to be made with extremely low F-numbers ($F/\# << 1$). However, the explicit solutions approximated according to ISO formula are solutions in a series with up to four deformation coefficients, which can have fast convergence or slow convergence ($O(r)$ o $o(r)$). There is not a formula that predicts a fast convergence for the parameters of the prescribed designs. In order to guarantee that the residual spherical aberration is below the diffraction limit, we recommend using a ray tracing by means of software.

Paraboloid surfaces are very common in optics, especially to design tunable mirrors [69]-[70] or fixed mirrors [73] manufactured by molding or spin casting. Note that a free surface of a rotating liquid in a gravitational field is a paraboloid, considering a small departure meniscus at the edge of the field generated by the hydrophilic or hydrophobic substrate. Sometimes, it can be practical to make paraboloid-aspheric lenses as substrate for mirrors, or use the same spin casting processes to make paraboloid surfaces of these lenses or inserts for plastic or glass molds.

Additionally, it is important to mention that there are many recent papers published concerning the refraction through singlet lenses to reduce the spherical aberration [74], [75],[76],[77],[78], trying to find the best corrective surfaces with an approach, which fits the ISO formula. So, we hope this work can help optical designers to do their work more quickly and easily.

Chapter 6

A numerical method to design lenses without spherical aberration

We present a numerical way to find the sign functions; that are necessary to know the equations to design any kind of singlet lenses without spherical aberration. It is valid for the case of real object and real image. It is showed a comparison between a theoretical model and the presented method.

The spherical aberration is one of the most studied monochromatic aberrations of an optical system. This is because the optimization of it can improve significantly the quality of the image on an optical axis. So, many researchers have studied this phenomenon: Roger Bacon identified it in spherical mirrors [79]. Later, J. Kepler (1611) and R. Descartes (1637) described it [80]. Descartes also studied the first lenses without spherical aberration, but he only considered the Cartesian ovals of revolution [22]. Afterwards, Luneburg proposed a method to avoid spherical aberration, but only for two particular cases [58]. Born and Wolf [3], Dijkterhuis [81], Hawking [82] and Ghatak [83] also studied the spherical aberration and described it.

Despite the many studies of spherical aberration, no one had been able to completely eliminate spherical aberration, until Valencia [37] proposed an analytical method for designing any kind of singlet lenses. As an example, he developed all analytic method to design spherical-aspheric and flat-aspheric lenses. Later, in [84] it is shown the same procedure for families of singlet paraboloid-aspheric lenses.

To apply the method to design singlet lenses free of all orders of spherical aberration is necessary to know the equations of the first surface and its derivative, the hard part is finding the signs functions involved in this method covering all possible cases for an specific family of singlet lenses. The authors of [37] and [84] have not described the method to find

these signs functions. So, the goal of this work is to propose a way to find these functions signs and consequently to have the analytic formulas to design any singlet lenses without spherical aberration supported by the Valencia's formulas.

Thus, following sections describes the method to obtain the function signs. In examples section, we present a comparison with the previous article ([84]). Finally discussions of the results are given.

6.1 Method

Singlet lens have two surfaces: z_a and z_b. Analytically any first surface z_a can be possible represented by

$$z_a(r_a) = \frac{c_a r_a^2}{1 + \sqrt{1 - (1 + K_a)\,(c_a r_a)^2}}\,, \tag{6.1}$$

where c_a is the curvature at vertex, K_a is conical constant according to Schwarzchild's representation [2] and r_a is a parameter that represents the height of the input ray.

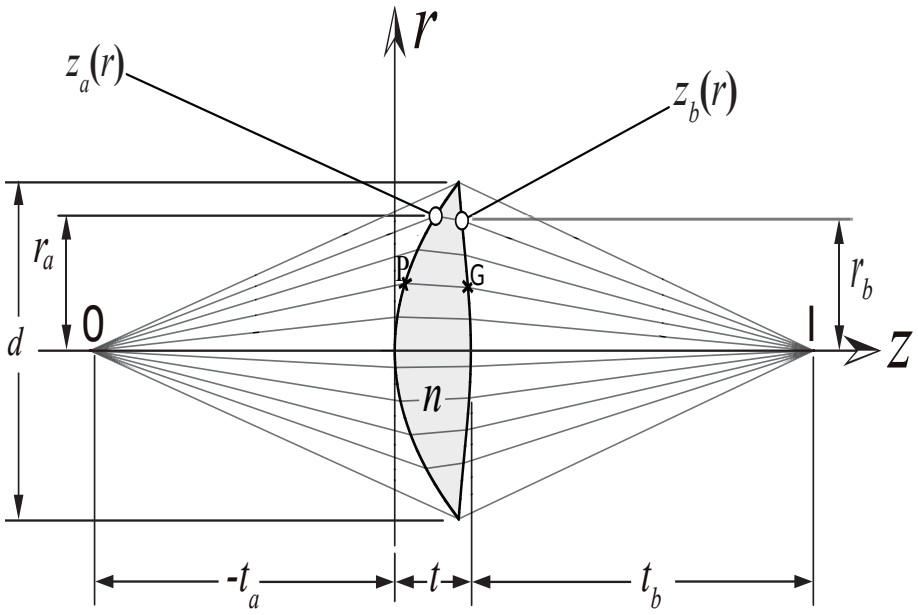

Figure 6.1: Design of any kind of singlet lens free of all orders of spherical aberration. The lens has a relative refractive index n, a first surface $z_a(r)$, a vertex anterior-object distance ta, a vertex-image point distance t_b, a maximal-aperture diameter d and center thickness t. O represents the object and I the image. P is a point in $z_a(r)$ and G is a point in $z_b(r)$. Assume the ray tracing from left to right and gaussian sign rule. The procedure will be described in the next section

Then, to find the second surface of a singlet lens without spherical aberration, we use parametric equation (r_b, z_b) given by Valencia´ s method:

$$r_b(r_a) = \left. \frac{B^2FG - s_4P(s_1EK + s_4N) + s_5 \ \text{sign}(r_a)\, B\sqrt{(FP - s_4G(s_1EK + s_4N))^2 + K(P^2 - B^2G^2)}}{B^2(F^2 + K) - (s_1EK + s_4N)^2} \right|_{r_a},$$

$$z_b(r_a) = t + t_b + \left. \frac{J - Ir - s_3|B|\sqrt{(G - Fr)^2 + (H^2 - B^2)r^2}}{H^2 - B^2} \right|_{r_a},$$

with letters A - R like recursive variables showed in [37]. All of these recursive variables are functions of the parameter r_a.

Note that there are signs functions s_1, s_3, s_4 and s_5, which can take dichotomic values. Therefore, there are 16 posibles formulas. So, we propose a simple way to select which of this posibles formulas (r_b, z_b) generate a lens without spherical aberration.

To determine the correct solution, we use the Fermat principe [2]. Let us consider any ray in Figure 1, for example $ray_1 = \overline{OP} + \overline{PG} + \overline{GI}$. By using Fermat principe the optical path of ray_1 which is $\overline{OP} + \overline{PG}\text{n} + \overline{GI}$ must be the same to $t_a + tn + t_b$.

On the other hand we obtain the optical path corresponding to each of the 16 posibles formulas for a particular ray (we choose the marginal ray). Then, we use the mean squared error between the above-mentioned optical path and the optical path of an axial ray $(t_a + tn + t_b)$. We name er to this error. Lastly, we select the formula that generates the minimum value of er.

Once having the sign functions, by ray tracing, we calculate the spot diagram to ensure that the design lens is corrected to the diffraction limit. This means we choose the correct sign functions.

Now, we present a example of our method in the next section to compare with [84].

6.2 Example

Using Eq. (6.1), we design a paraboloid-aspherical lens with the following parameters: $n = 1.5$, $R_a = 50$mm, $tb = 100$mm, $t = 10$mm, $t_a = -100$, $d_l = 46.09753$mm. Figure (6.2) shows the two profiles of the designed lens. z_b varies depending on signs. Using the

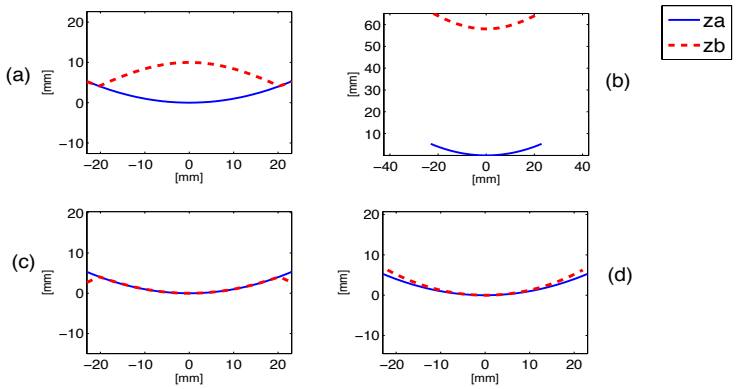

Figure 6.2: Design of paraboloid-aspherical biconvex lens, where the object is real and the image is real too. The parameters of this lens are: $n = 1.5$, $R_a = 50$mm, $tb = 100$mm, $t = 10$mm, $t_a = -100$, $d_l = 46.09753$mm.

proposed method, we find that $s1 = 1$, $s5 = 1$. This implies that the profiles of the lens are those drawn in Figure (6.2 a) These results agree with the analytical method.

6.3 Conclusion

We proposed a numerical method to find the formulas to design any kind of singlet lenses without spherical aberration. We compared this method with an analytic method for paraboloid-aspheric lenses; these two methods converge to the same function for the case: real object and real image.

The next step is to propose a numerical method to find the sign functions for the three missing cases (real object-virtual image, virtual object-real image, virtual object-virtual image) and thus generalize the numerical method.

Chapter 7

General discussion

Unlike work [33], this thesis shows an analytical lens design to generate super-resolving properties. We have not found reports about optical design of lenses with super-resolution characteristics . Therefore, for the first time an analytical design for the design of lenses with super-resolving properties is shown.

In this chapter the contributions of this work are explained more in detail.

7.1 Theory of thickness

Following an extended procedure of Goodman [6], a thick lens can be represented by the phase function given by

$$g(r) = e^{ikt_c} e^{ik(n_l - n_a)t(r)} \tag{7.1}$$

where $t(r)$ is the lens axial thickness at abscissa, $r = \sqrt{x^2 + y^2}$, t_c is the center thickness of the lens, n_l and n_a with $n_a < n_l$ are the refractive indexes of the lens and its surrounding media, respectively.

It can be noted that our proposal is more general than proposal of Goodman. In Goodman's work, where the following analysis is made:

Let the máximum thickness of the lens and let the thickness at radial coordinates r be t(r). Then the total phase delay suffered by the wave at coordinates r introduced by the lens may be written by

$$\phi(x, y) = knt(r) + k(t_0 - t(r)) \tag{7.2}$$

where n is the refractive index of the lens material. The thickness function is obtained splitting the lens into three parts to obtained

$$t(r) = t_0 - R_1(1 - \sqrt{1 - \frac{r^2}{R_1^2}}) + R_2(1 - \sqrt{1 - \frac{r^2}{R_2^2}}) \tag{7.3}$$

The above equation can be simplified using the following paraxial approximation

$$\begin{aligned} \sqrt{1 - \frac{r^2}{R_1^2}} &\approx 1 - \frac{r^2}{2R_1^2} \\ \sqrt{1 - \frac{r^2}{R_2^2}} &\approx 1 - \frac{r^2}{2R_2^2} \end{aligned} \tag{7.4}$$

So, Equation (7.3) changes to

$$t(r) = t_0 - \frac{r^2}{2}(\frac{1}{R_1} - \frac{1}{R_2}). \tag{7.5}$$

And using the following equation

$$\frac{1}{f} = (n - 1)(\frac{1}{R_1} - \frac{1}{R_2}), \tag{7.6}$$

the paraxial representation of a thin lens is obtained, which is given analytically as

$$g(r) = e^{\frac{-ik}{2f}r^2} \tag{7.7}$$

We note that this expression is considerably simpler and less accurate than our non-paraxial expression.

7.2 Super-resolving pupil used

The first step of the process consists in proposing the super-resolving functions, for instance,

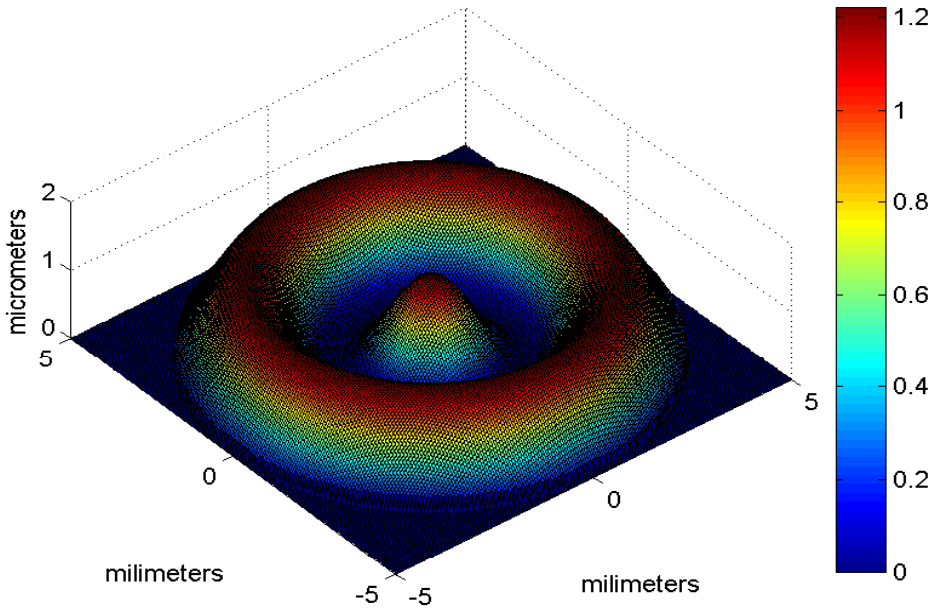

Figure 7.1: Super-resolving function $\tilde{z}_b$ of a flat-hyperbolic lens

$$\tilde{z}_b(r) = b_1[1 + cos(b_2 2\pi r)]/[k(n_l - n_a)] \tag{7.8}$$

where b_1 and b_2 are parameters to be optimized. Some paraxial super-resolving pupil designs using this function have been reported in [34]. Unlike Cagigal, we find that b1 and b2 are not constants but parameters that depend on the diameter of the lenses and their shape (flat-hyperbolic, biconvex, etc.).

In order to show the shape of the surface $\tilde{z}_b$ that should be added to the second surface, we will take as an example the flat-hyperbolic lens, which was described in chapter 4 and it has a diameter of 10 mm. The shape of the surface $\tilde{z}_b$ is showed in Figure (7.1). It can be noted that $\tilde{z}_b$ has maximum changes of 1.2 micrometers.

The Wyko can solve at most 12 rings, which translated to units of son length approximately 3.8 micrometers. That is to say that between peak-valley greater than 3.8 micrometers.

It should be mentioned that the Wyko interferometer was ideally designed to measure flat and spherical surfaces, but not aspherical. Therefore, when measuring aspheric surfaces certain limitations, such as those mentioned above, occur.

7.3 Experimental data with amplitude pupil

To test experimentally the theory of thickness function and its application in the design of super-resolving lenses, we placed several pupils of amplitude of different diameters in the lens that was previously manufactured. The purpose was to establish a non-paraxial relationship between the diameter of the pupil, normalized to the real diameter of the lens, and the reduction of its PSF and check with the theory we developed. We had to find the degree of correlation between theory and experiment. In this stage we have the experimental results of PSFs corresponding to 25 different diameters, however, we did not make the comparison. In general, we can mention that effectively, by increasing the diameter of the amplitude pupil, the diameter of the central disc of the PSF is reduced, the amplitude of the secondary lobes is increased and the Strehl ratio is reduced.

It is worth mentioning that in [3] a paraxial study of this phenomenon is made. In this work, the diffraction of an annular pupil is analyzed and explained below:

Suppose that the annular aperture is bounded by two concentric circles of radius a and ϵa , where ϵ is some positive number less than unity. Then, the light distribution in the Fraunhofer pattern is represented by

$$G(u) = 2\int_0^a J_0(u\rho)\rho \mathrm{d}\rho - 2\int_0^{\epsilon a} J_0(u\rho)\rho \mathrm{d}\rho \tag{7.9}$$

where a is the radius of lens, J_0 is Bessel function of order cero.

Then, the intensity is given by

$$I(u) = |G(u)|^2 = \frac{I_0}{(1-\epsilon^2)^2}\left[\frac{2J_1(aw)}{aw} - \epsilon^2\frac{2J_1(\epsilon aw)}{\epsilon aw}\right]^2 \tag{7.10}$$

where $I_0 = a^4(1-\epsilon^2)^2$ is the intensity at center $w = 0$ of the pattern. The positions of the zeros of intensity are given by the roots of the following equation

$$J_1(aw) - \epsilon J_1(\epsilon aw) = 0 \tag{7.11}$$

As ϵ is increased, the first rood of Equation (7.11) decreases, which means that its Airy disk decreases. From $I_0 = a^4(1-\epsilon^2)^2$, it is evident that the central intensity has its maximum at $\epsilon = 1$.

We have the experimental data, we want to find a numerical relation between ϵ, reduction of Airy disc and increase of secondary lobe. Actually, we used data to made qualitative analysis, but the quantitative analysis is left as future work.

7.4 Utility range

In this work we can notice that Equation (7.1) (exact lenses) do not have any limitation regarding the diameter of the lenses or the focal distance of them; that is, they are not limited to a paraxial development. Similarly, the fact that we have used the Rayleigh-Sommerfeld diffraction represented by Equation (4.7) to find the super-resolution function, we do not have any restrictions either. In this sense, We can design lenses from millimeters to meters, since method do not have restrictions. The complexity, of course, it will be its manufacture.

7.5 Simulated images with super resolution

An image is the result of the convolution of the PSF with the object. As a demonstration, it compares two images: in one the PSF has a smaller Airy disk than the other. Depending on the parameter ϵ, it is the size of the Airy disk. Figure (7.2) showed two PSF's with different size of Airy disc. These PSF's were used to generate the images showed in Figure (7.3). The image showed in a), it is the resulting image using the PSF shown in Figure (7.2 (a)). Image showed in Figure (7.3 (b)) is the resulting image using the PSF shown in Figure (7.2 (b)). Figure (7.3 (c)) is the original image.

It can be noticed that the image resulting from the convolution with a PSF with a smaller Airy disk has more defined edges. This is because the mathematical operation convolution is an average. If the size of the filter is larger then the image becomes more blurred as shown in Figure (7.3 (b)).

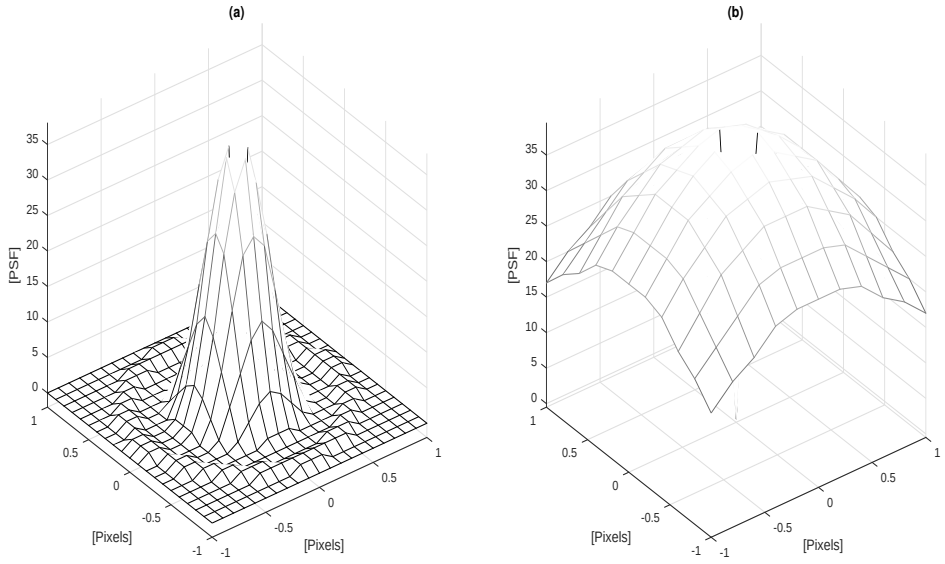

Figure 7.2: PSF's. PSF showed in a) has Airy disc smaller than PSF showed in b).

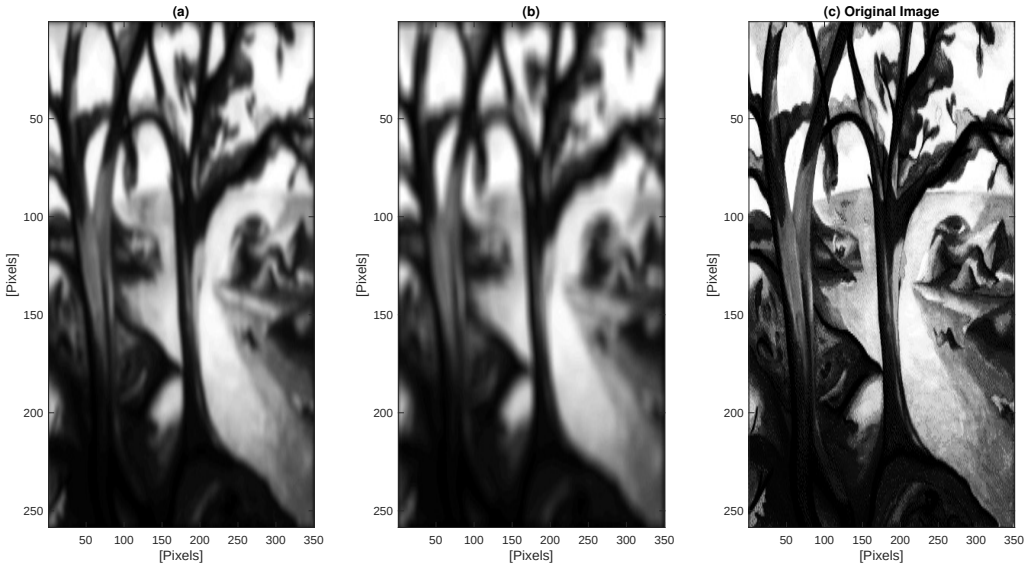

Figure 7.3: Images as convolution

7.6 Congruence of the themes

We may wonder why we use exact equations with spherical aberration corrected on the optical axis. The reason was that in order to introduce the super-resolution we must first have the optical systems limited by diffraction since it does not make sense to improve an aberrated PSF. As an aberrated PSF increases its dimensions with the aberrations.

Then, it is very important to reduce or eliminate the aberrations. Since we worked in the optical axis, we consider that it is enough to eliminate the spherical aberration, since it is the only aberration that affects the optical axis.
We want to make our study more general. A method to generate lenses with super-resolution properties not only in axis, but the analysis is more complex, since we must consider other aberrations. So, it is also left as future work.

7.7 Aspherical lens manufactured

Regarding the lens designed and manufactured by CIO, it is a flat-hyperbolic lens. Since we consider that a flat surface is easier to incorporate another surface (super-resolving function), which acts as the super-resolving function. The lens is designed so that the hyperbolic surface between the collimated beam and the flat part focuses the beam at a point. First, the lens is designed to the diffraction limit.

It should be mentioned that the hyperbolic-plane lens limited by diffraction was manufactured by the aspheres lens polishing machine, recently acquired by the Cio and the lens is one of the first lenses manufactured by that machine. Figure (7.4) shows Zeeko lens polishing machine.

The manufacturing process of the lens will be briefly described below. First a block of glass is cut, then with the help of the polishing machine shown in Figure (7.5) a spherical lens is manufactured, which is polished by the traditional method. Pitch molds are made, shown in Figure (7.6), and placed in a lathe machine , which causes the surface of the lens with the pitch mold to be kept in a homogeneous friction by all the surface.

To generate the lens design in Wyko Software, it is necessary only seven terms of asphericity, whereas the Zeeko Software has 20 terms of asphericity. Figure (7.7) shows the aforementioned Software interface.

When the spherical lens is ready, it proceed to program the Zeeko polishing machine, which automatically makes the lens disguises, since the lens has a profile as shown in Figure

Figure 7.4: Zeeko lens polishing machine

(a) (b)

Figure 7.5: Generating machine.a) Machine,b) How mechanical tool makes contact with glass to generate a spherical lens.

(a) (b)

Figure 7.6: Process of polishing lens

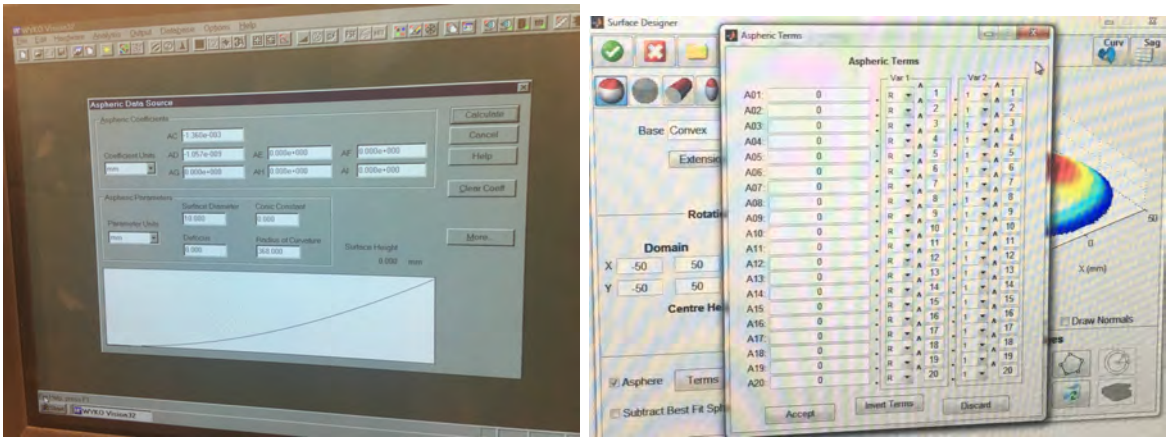

(a) (b)

Figure 7.7: Software Interface, a) Wyko , b) Zeeko

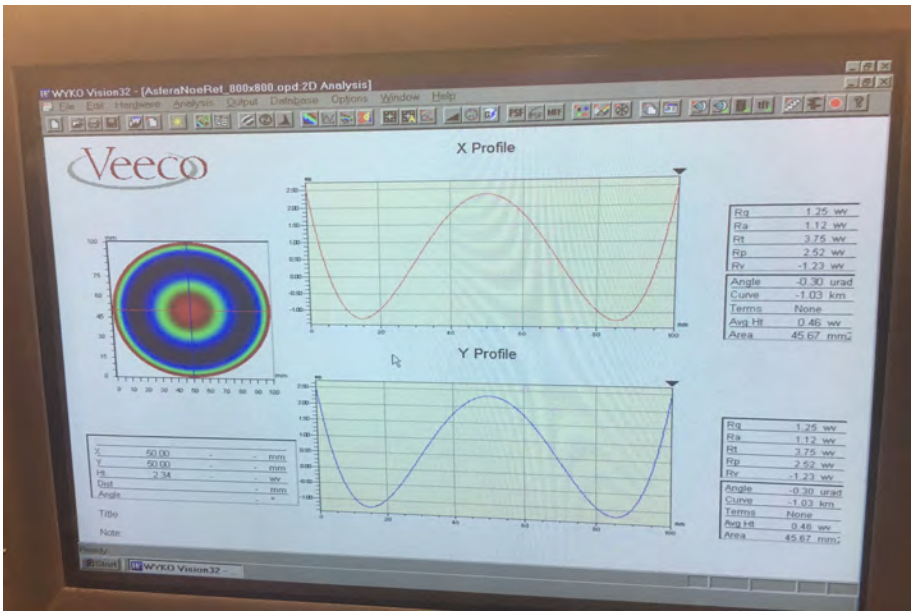

Figure 7.8: Wyko interface of aspherical surface

(7.8). Zeeko machine.

The machine is generating the profile that is requested in the Software, but often it does not devastate the material well where it should be done. Therefore, when a first disguise was made, the lens is measured in the Wyko interferometer, in order to analyze if it is the required lens. For this a comparison is made between the lens generated by Zeeko and the ideal lens, which is designed by the Wyko Software.

If the manufactured lens differs a lot from the designed one, then it will be return again in the Zeeko machine, then it will be measured again in the Wyko until a difference between the two tolerable lenses is achieved.

Experimentally, it is known that the values of the coefficients of asphericity must not exceed certain ranges, since the Zeeko machine can not understand them and it seems that it is locked.

For demonstration purposes that our method works, the method is applied to lenses; we consider that it is easier to work with a flat surface than a curved surface. In which we will add our super-resolution function. It is for this reason that it do not work with mirrors.

Chapter 8

General conclusions and future directions

It is important to generate super-resolution in various optical systems that are used on a daily basis. Many areas such as biology, chemistry, medicine, genetics benefit from advances in super-resolution, as this allowed to humanity analyze smaller objects for the advance of science and technology improving the quality of the life.

The lens is the simplest optical system; thus, we chose to devote ourselves to developing a method to generate super-resolution in a lens. In this thesis it was demonstrated theoretically and analytically the performance of the method. We proposed a method to generate super-resolved lenses by modifying one surface of the lens. This allowed the PSF to be reduced. This means that optical systems can solve smaller objects, that is, they are super-resolving systems. To achieve this we started the method using lenses without spherical aberration, which were previously designed by other authors. Some examples are shown.

To generate super-resolution is necessary to correct the aberrations, that is the reason why this work is also dedicated to the reduction of spherical aberration in lenses, since this aberration is the most difficult to correct.

We designed a corrected lens at the diffraction limit. It was fabricated. We tested the lens with Wyko interferometer to prove the correction to the diffraction limit. Later, we used amplitude pupils to show the super-resolution behavior.

Once the purpose of generating super-resolution lenses was achieved, we decided to go one step further, that is, to find the mathematical formulas to generate parabolic-aspherical lenses without spherical aberration. This in order to generate a more general method to design any type of super-resolution lenses. The reason for choosing these types of lenses was

because they are widely used in various applications, which translates to a work with impact.

The next step will be design a super-resolving lenses by using the paraboloid-aspherical lenses.

Bibliography

[1] Olvera Daniel. Estudio de la super-resolución óptica en microscopía holográfica de gabor. Master's thesis, Centro de Investigaciones en Optica, A. C., 2014.

[2] Daniel Malacara and Zacarias Malacara. Handbook of optical design, 2004.

[3] Max Born and Emil Wolf. *Principles of optics: electromagnetic theory of propagation, interference and diffraction of light*. Elsevier, 2013.

[4] Arnold Sommerfeld. *Lectures on theoretical physics: Optics*, volume 4. Academic Press, 1964.

[5] Noé Alcalá Ochoa. Alternative approach to evaluate the rayleigh-sommerfeld diffraction integrals using tilted spherical waves. *Optics Express*, 25(10):12008–12019, 2017.

[6] Joseph W Goodman. *Introduction to Fourier optics*. Roberts and Company Publishers, 2005.

[7] Wolfgang Singer, Michael Totzeck, and Herbert Gross. *Handbook of optical systems, physical image formation*, volume 2. John Wiley & Sons, 2006.

[8] Carroll Mason Sparrow. On spectroscopic resolving power. *The Astrophysical Journal*, 44:76, 1916.

[9] Stefan W Hell. Microscopy and its focal switch. *Nature methods*, 6(1):24–32, 2009.

[10] Ernst Abbe. Beiträge zur theorie des mikroskops und der mikroskopischen wahrnehmung. *Archiv für mikroskopische Anatomie*, 9(1):413–418, 1873.

[11] Marcel A Lauterbach. Finding, defining and breaking the diffraction barrier in microscopy–a historical perspective. *Optical nanoscopy*, 1(1):8, 2012.

[12] José Sasián. *Introduction to aberrations in optical imaging systems*. Cambridge University Press, 2013.

[13] Colin JR Sheppard. Fundamentals of superresolution. *Micron*, 38(2):165–169, 2007.

[14] Aaron Lewis, Hesham Taha, Alina Strinkovski, Alexandra Manevitch, Artium Khatchatouriants, Rima Dekhter, and Erich Ammann. Near-field optics: from subwavelength illumination to nanometric shadowing. *Nature biotechnology*, 21(11):1378–1386, 2003.

[15] Mats GL Gustafsson. Surpassing the lateral resolution limit by a factor of two using structured illumination microscopy. *Journal of microscopy*, 198(2):82–87, 2000.

[16] Stefan W Hell, Steffen Lindek, Christoph Cremer, and Ernst HK Stelzer. Confocal microscopy with an increased detection aperture: type-b 4pi confocal microscopy. *Optics letters*, 19(3):222–224, 1994.

[17] Rainer Heintzmann and Gabriella Ficz. Breaking the resolution limit in light microscopy. *Briefings in Functional Genomics*, 5(4):289–301, 2006.

[18] Vicente Mico, Zeev Zalevsky, Carlos Ferreira, and Javier García. Superresolution digital holographic microscopy for three-dimensional samples. *Optics express*, 16(23):19260–19270, 2008.

[19] Robert Jones and Catherine Wykes. *Holographic and speckle interferometry*, volume 6. Cambridge university press, 1989.

[20] Fu-Pen Chiang. Super-resolution digital speckle photography for micro/nano measurements. *Optics and Lasers in Engineering*, 47(2):274–279, 2009.

[21] Juanjuan Zheng, Giancarlo Pedrini, Peng Gao, Baoli Yao, and Wolfgang Osten. Autofocusing and resolution enhancement in digital holographic microscopy by using speckle-illumination. *Journal of Optics*, 17(8):085301, 2015.

[22] René Descartes. Discours de la méthode pour bien conduire sa raison, et chercher la verité dans les sciences. plus la dioptrique. les meteores. et la geometrie. qui sont des essais de cette methode, 1637.

[23] Juan Camilo Valencia Estrada, Álvaro Hernán Bedoya Calle, and Daniel Malacara Hernández. Explicit representations of all refractive optical interfaces without spherical aberration. *JOSA A*, 30(9):1814–1824, 2013.

[24] Rudolf Kingslake and R Barry Johnson. *Lens design fundamentals*. academic press, 2009.

[25] G Toraldo Di Francia. Super-gain antennas and optical resolving power. *Il Nuovo Cimento (1943-1954)*, 9(3):426–438, 1952.

[26] Tasso RM Sales. Smallest focal spot. *Physical review letters*, 81(18):3844, 1998.

[27] Noé Alcalá Ochoa and Carlos Pérez-Santos. Super-resolution with complex masks using a phase-only lcd. *Optics letters*, 38(24):5389–5392, 2013.

[28] Jari Lindberg. Mathematical concepts of optical superresolution. *Journal of Optics*, 14(8):083001, 2012.

[29] Ninfa del C Lozano-Rincón and Noé Alcalá Ochoa. Design of super-resolving lenses in far-field imaging. *Optics Communications*, 383:316–322, 2017.

[30] Vidal F Canales, Pedro J Valle, Jose E Oti, and Manuel P Cagigal. Pupil apodization for increasing data storage density. *Chinese Optics Letters*, 7(8):720–723, 2009.

[31] Haifeng Wang, Zhongyu Chen, and Fuxi Gan. Phase-shifting apodizer for next-generation digital versatile disk. *Optical Engineering*, 40(6):991–994, 2001.

[32] Francisco J Martínez, Andrés Márquez, Sergi Gallego, Jorge Francés, Inmaculada Pascual, and Augusto Beléndez. Retardance and flicker modeling and characterization of electro-optic linear retarders by averaged stokes polarimetry. *Optics letters*, 39(4):1011–1014, 2014.

[33] Yat Hei Lo and Rainer Leonhardt. Aspheric lenses for terahertz imaging. *Optics express*, 16(20):15991–15998, 2008.

[34] Manuel P Cagigal, Vidal F Canales, and José E Oti. Design of continuous superresolving masks for ground-based telescopes. *Publications of the Astronomical Society of the Pacific*, 116(824):965, 2004.

[35] Noé Alcalá Ochoa, J García-Márquez, and A González-Vega. Hybrid pupil filter design using bessel series. *Optics Communications*, 284(20):4900–4902, 2011.

[36] Vidal F Canales and Manuel P Cagigal. Pupil filter design by using a bessel functions basis at the image plane. *Optics express*, 14(22):10393–10402, 2006.

[37] Juan Camilo Valencia-Estrada, Ricardo Benjamín Flores-Hernández, and Daniel Malacara-Hernández. Singlet lenses free of all orders of spherical aberration. In *Proc. R. Soc. A*, volume 471, page 20140608. The Royal Society, 2015.

[38] Warren J Smith. *Modern optical engineering*. Tata McGraw-Hill Education, 1966.

[39] *ISO 10110-1996, Optics Drawing Standards for the National Ignition Facility.*

[40] David D Walker, Richard Freeman, Gerry McCavana, Roger Morton, David Riley, John Simms, David Brooks, ED Kim, and Andrew King. The zeeko/ucl process for polishing large lenses and prisms. In *Proc. SPIE*, volume 4411, pages 106–111, 2002.

[41] I Leiserson, SG Lipson, and V Sarafis. Superresolution in far-field imaging. *Optics letters*, 25(4):209–211, 2000.

[42] Hongxin Luo and Changhe Zhou. Comparison of superresolution effects with annular phase and amplitude filters. *Applied optics*, 43(34):6242–6247, 2004.

[43] Salvador Alejandro Juárez-Reyes, Paula Ortega-Vidals, and Gilberto Silva-Ortigoza. Wavefronts, light rays and caustic associated with the refraction of a spherical wave by two interfaces: the axicon and the plano-convex parabolic lenses. *Journal of Optics*, 17(6):065604, 2015.

[44] Hutchins N. F. Enhancing fso link performance in adverse conditions using a fiber-bundle based receiver design. Master's thesis, The University of Tulsa, 2015.

[45] T.; Benech P. Rooms, F.; Gonthiez. *Systeme Optique Transmissif a Caracteristiques Variables*, 2008.

[46] Antonin Miks, Jiri Novak, and Pavel Novak. Algebraic and numerical analysis of imaging properties of thin tunable-focus fluidic membrane lenses with parabolic surfaces. *Applied optics*, 52(10):2136–2144, 2013.

[47] Zhenxian Zhan, Keyi Wang, Haitao Yao, and Zhaolou Cao. Fabrication and characterization of aspherical lens manipulated by electrostatic field. *Applied optics*, 48(22):4375–4380, 2009.

[48] Can L. Zancheng L. *Superthin hyperbolic paraboloid lens for spectacles.* Espacenet CN2098696(U). 19910223., 1992.

[49] William M Berke. Orthokeratological contact lenses and design methods therefor, November 24 2011. US Patent App. 13/162,303 US7984989 (B2).

[50] William M Berke. Orthokeratological contact lenses and design methods therefor, June 16 2011. US Patent App. 13/162,303 US7984988 (B2).

[51] Sergio Barbero, Susana Marcos, Javier Montejo, and Carlos Dorronsoro. Design of isoplanatic aspheric monofocal intraocular lenses. *Optics express*, 19(7):6215–6230, 2011.

[52] Blechinger Fritz Gross, Herbert and Bertram Achtner. *Handbook of Optical Systems, Survey of Optical Instruments*, volume 4. Wiley-VCH, 2008.

[53] H Knuppertz, M Bohling, and J Jahns. Mikrooptische realisation eines pulsformers für femtosekundenpuls-anwendungen. *Proceedings of the DGaO, Stuttgart*, 2007.

[54] Bruno Lengeler, Christian Schroer, Johannes Tümmler, Boris Benner, Matthias Richwin, Anatoly Snigirev, Irina Snigireva, and Michael Drakopoulos. Imaging by parabolic refractive lenses in the hard x-ray range. *Journal of Synchrotron Radiation*, 6(6):1153–1167, 1999.

[55] Markus Simon. *Röntgenlinsen mit großer Apertur*. KIT Scientific Publishing, 2014.

[56] Sven Kiontke, Marcel Demmler, Michael Zeuner, Frank Allenstein, Thoralf Dunger, and Matthias Nestler. Ion-beam figuring (ibf) for high-precision optics becomes affordable. In *Current Developments in Lens Design and Optical Engineering XI; and Advances in Thin Film Coatings VI*, volume 7786, page 77860F. International Society for Optics and Photonics, 2010.

[57] Woei Ming Lee. Fabricating lenses using gravity, January 30 2015. US Patent App. 15/115,180.

[58] Rudolf Karl Luneburg and Max Herzberger. *Mathematical theory of optics*. Univ of California Press, 1964.

[59] GD Wassermann and E Wolf. On the theory of aplanatic aspheric systems. *Proceedings of the Physical Society. Section B*, 62(1):2, 1949.

[60] Orestes N Stavroudis. *The mathematics of geometrical and physical optics: the k-function and its ramifications*. John Wiley & Sons, 2006.

[61] David L Shealy and John A Hoffnagle. Wavefront and caustics of a plane wave refracted by an arbitrary surface. *JOSA A*, 25(9):2370–2382, 2008.

[62] John A Hoffnagle and David L Shealy. Refracting the k-function: Stavroudis's solution to the eikonal equation for multielement optical systems. *JOSA A*, 28(6):1312–1321, 2011.

[63] HA Buchdahl. Optical aberration coefficients. viii. coefficient of spherical aberration of order eleven. *JOSA*, 50(7):678–683, 1960.

[64] HA Buchdahl. Optical aberration coefficients. xii. remarks relating to aberrations of any order. *JOSA*, 55(6):641–649, 1965.

[65] Robert T Jones. Wide angle lenses with aspheric correcting surfaces. *Applied optics*, 5(11):1846–1849, 1966.

[66] Orestes N Stavroudis. Two-surface refracting systems with zero third-order spherical aberration. *JOSA*, 59(3):288–293, 1969.

[67] NE Ellis and WT Welford. Applications of aspheric optics in laser fusion. In *Society of Photo-Optical Instrumentation Engineers (SPIE) Conference Series*, volume 235, pages 18–20, 1981.

[68] Maxim E Frolov, Alexei M Khorokhorov, Alexander F Shirankov, and Yuri B Golubkov. Design of aplanatic singlet for pickup. In *International Symposium on Optical Memory and Optical Data Storage*, page WP1. Optical Society of America, 2005.

[69] Sjoerd Stallinga. Finite conjugate spherical aberration compensation in high numerical-aperture optical disc readout. *Applied optics*, 44(34):7307–7312, 2005.

[70] JC Valencia and R Flores. Lentes correctoras y método para producirlas con cero aberración esférica. Technical report, PCT/MX/2013/000141, WIPO, 2012.

[71] Hans-Christoph Im Hof and Ernst A Ruh. An equivariant pinching theorem. *Commentarii Mathematici Helvetici*, 50(1):389–401, 1975.

[72] Chun Li Shen. A global pinching theorem of minimal hypersurfaces in the sphere. *Proceedings of the American Mathematical Society*, 105(1):192–198, 1989.

[73] Wolfram MathWorld. The web's most extensive mathematics resource, 2010.

[74] YiQuan Liu, ChenGuang Zhang, and JianGuo Xin. Low spherical aberration of the focal length tunable liquid lens. In *Selected Papers from Conferences of the Photoelectronic Technology Committee of the Chinese Society of Astronautics 2014, Part I*, volume 9521, page 952105. International Society for Optics and Photonics, 2015.

[75] Suryakant Gautam, Amit Gupta, and GS Singh. Comparative assessment of optical performance for the optical design of hd-dvd micro objective lens with na 0.65 using aspheric and freeform surfaces. *Optik-International Journal for Light and Electron Optics*, 125(22):6845–6849, 2014.

[76] M Sunohara, Y Tanaka, Y Nagaoka, M Ueda, and K Azuma. Single lens cd player pickup system using a bi-aspheric molded glass lens. *IEEE transactions on consumer electronics*, (4):520–530, 1987.

[77] Gabriel Castillo-Santiago, Maximino Avendaño-Alejo, Rufino Díaz-Uribe, and Luis Castañeda. Analytic aspheric coefficients to reduce the spherical aberration of lens elements used in collimated light. *Applied optics*, 53(22):4939–4946, 2014.

[78] Gabriel Castillo, Maximino Avendaño-Alejo, and J Rufino Diaz-Uribe. Analytic aspheric coefficients to reduce the spherical aberration. In *Latin America Optics and Photonics Conference*, pages LTh3B–5. Optical Society of America, 2014.

[79] Moritz Von Rohr. Geometrical investigation of the formation of images in optical instruments. *Geometrical Investigation of the Formation of Images in Optical Instruments by M. Von Rohr London, GB: His Majesty's Stationary Office, 1920*, 1920.

[80] Henry C King. *The history of the telescope*. Courier Corporation, 1955.

[81] Fokko Jan Dijksterhuis. *Lenses and waves: Christiaan Huygens and the mathematical science of optics in the seventeenth century*, volume 9. Springer Science & Business Media, 2006.

[82] S Hawking. René descartes. *God created the integers: the mathematical breakthroughs that changed history*, page 285, 2005.

[83] Ghatak A. *Optics*. McGraw-Hill, 1939.

[84] Ninfa del C Lozano-Rincón and Juan Camilo Valencia-Estrada. Paraboloid–aspheric lenses free of spherical aberration. *Journal of Modern Optics*, 64(12):1146–1157, 2017.